ATLAS Paper Draft
ANA-HDBS-2019-08
Version 0.3
Target journal: JHEP

Comments are due by: To be added

Supporting internal notes

4ℓ+MET internal note: https://cds.cern.ch/record/2788797

Search for heavy resonances in final states with 4ℓ and missing transverse energy or jets in pp collisions at $\sqrt{s} = 13$ TeV with the ATLAS detector

A search for a new heavy boson produced via gluon-fusion in the four-lepton channel with missing transverse energy or jets is performed. The search uses proton-proton collision data equivalent to an integrated luminosity of 139 fb^{-1} at a centre-of-mass energy of 13 TeV collected by the ATLAS detector between 2015 and 2018 at the Large Hadron Collider. The heavy boson, R or A, decays to an S or Z boson and to another heavy Higgs-like boson, H, which decays into two Z bosons. The S boson is assumed to decay to dark matter, and the associated Z boson decays either to two leptons or inclusively. The mass range of the heavy boson studied is 390–1300 (320–1300) GeV for the R (A) boson and 220–1000 GeV for the H boson. The mass of the S boson is fixed at 160 GeV. No significant deviation from the Standard Model backgrounds is observed. The results are interpreted as upper limits at a 95% confidence level on the $\sigma(gg \to R) \times \mathcal{B}(R \to SH) \times \mathcal{B}(H \to ZZ) \times \mathcal{B}(ZZ \to 4\ell)$ and $\sigma(gg \to A) \times \mathcal{B}(A \to ZH) \times \mathcal{B}(H \to ZZ) \times \mathcal{B}(ZZZ \to 4\ell)$. The observed (expected) upper limits are in the range of 0.031–0.539 (0.034–0.343) fb for the $R \to SH \to 4\ell + E_{\mathrm{T}}^{\mathrm{miss}}$ signal and 0.027–0.419 (0.035–0.335) for the $A \to ZH \to 4\ell + X$ signal.

Document created on 7th August 2023 using ATLAS LaTeX Version 07-03-00.

Analysis Team

[*email:* atlas-ana-hdbs-2019-08-editors@cern.ch]

Abdualazem Fadol, Yaquan Fang, Theodota Lagouri, Bruce Mellado, Onesimo Mtintsilana, Xifeng Ruan, Humphry Tlou, R D Schaffer

Editorial Board

[*email:* atlas-ana-hdbs-2019-08-editorial-board@cern.ch]

Klaus MONIG (DESY) (chair)
Yusheng WU (Hefei)
Haider ABIDI (Brookhaven BNL)

ATLAS EXPERIMENT
Journal: JHEP

ATLAS Paper

ANA-HDBS-2019-08

7th August 2023

CERN
Draft version 0.3

Search for heavy resonances in final states with 4ℓ and missing transverse energy or jets in pp collisions at $\sqrt{s} = 13$ TeV with the ATLAS detector

The ATLAS Collaboration

A search for a new heavy boson produced via gluon-fusion in the four-lepton channel with missing transverse energy or jets is performed. The search uses proton-proton collision data equivalent to an integrated luminosity of 139 fb^{-1} at a centre-of-mass energy of 13 TeV collected by the ATLAS detector between 2015 and 2018 at the Large Hadron Collider. The heavy boson, R or A, decays to an S or Z boson and to another heavy Higgs-like boson, H, which decays into two Z bosons. The S boson is assumed to decay to dark matter, and the associated Z boson decays either to two leptons or inclusively. The mass range of the heavy boson studied is 390–1300 (320–1300) GeV for the R (A) boson and 220–1000 GeV for the H boson. The mass of the S boson is fixed at 160 GeV. No significant deviation from the Standard Model backgrounds is observed. The results are interpreted as upper limits at a 95% confidence level on the $\sigma(gg \to R) \times \mathcal{B}(R \to SH) \times \mathcal{B}(H \to ZZ) \times \mathcal{B}(ZZ \to 4\ell)$ and $\sigma(gg \to A) \times \mathcal{B}(A \to ZH) \times \mathcal{B}(H \to ZZ) \times \mathcal{B}(ZZZ \to 4\ell)$. The observed (expected) upper limits are in the range of 0.031–0.539 (0.034–0.343) fb for the $R \to SH \to 4\ell + E_{\mathrm{T}}^{\mathrm{miss}}$ signal and 0.027–0.419 (0.035–0.335) for the $A \to ZH \to 4\ell + X$ signal.

Contents

1 Introduction

In 2012, the ATLAS and CMS experiments independently discovered a new particle [1, 2]. The new particle's properties are consistent with the Higgs boson proposed by the Standard Model (SM) [3–6]. However, the SM still has several open questions, including dark matter, neutrino masses and mixing, the hierarchy problem, and the strong CP problem [7–9]. It is still debated whether the Higgs boson is a standalone particle or part of the Higgs sector suggested by the two-Higgs-doublet model (2HDM) [10, 11]. The 2HDM predicts the existence of five Higgs bosons, including a CP-even particle like the SM Higgs boson (h), a heavier Higgs boson (H), a CP-odd particle (A), and a charged Higgs scalar ($H^{\pm}$). Another extension to the SM is the 2HDM+S model, which introduces a scalar boson (S) assumed to be a dark matter portal and a possible source of missing transverse energy [12, 13].

This paper aims to search for heavy resonances that decay to 4ℓ and missing transverse energy or jets, focusing on the high-mass region of the heavy bosons where the four-lepton invariant mass is above 200 GeV. This study uses proton-proton collision data at a centre-of-mass energy of 13 TeV and integrated

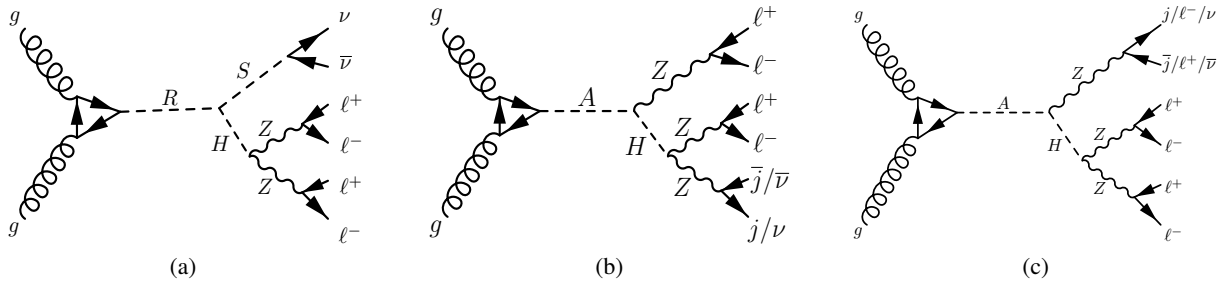

Figure 1: Feynman diagrams represent the production of heavy bosons via gluon-fusion at leading-order for the (a) $R \to SH \to 4\ell + E_{\mathrm{T}}^{\mathrm{miss}}$ signal, (b) $A \to Z(\to 2\ell)H(\to 2\ell + j\bar{j}/\nu\bar{\nu})$ signal, and (c) $A \to Z(\to j\bar{j}/\ell^{+}\ell^{+}/\nu\bar{\nu})H(\to 4\ell)$ signal, where ℓ could either be an electron or a muon, j represents a jet and ν denotes the SM neutrino.

luminosity of 139 fb^{-1} collected by the ATLAS detector in the 2015–2018 period at the Large Hadron Collider (LHC). Two different scenarios are considered for the signal model. First, the 2HDM+S model only includes a heavy resonance H and Higgs-like scalar boson S. The model is extended to cover more general situations for various missing energy magnitudes by adding one heavy scalar R, where R decays to H and S bosons with $m_R > m_H + m_S$. The S boson decays into dark matter particles ($S \to \nu\nu$), and the H decays to 4ℓ through the decay of two Z bosons ($H \to ZZ \to 4\ell$). The masses of the R and H bosons are varied to control the missing transverse energy, and the S mass is fixed to 160 GeV. The assumption of the S mass is motivated by the phenomenology study presented in Ref. [14]. However, we studied the effect of this choice and found that the S mass only affects the distribution of the missing transverse energy if its mass is above 200 GeV. Therefore, fixing the S mass reduces the free parameters on the fit and simplifies the analysis. The phenomenology of the new $R \to SH$ topology can easily embed into the 2HDM+S model using a similar approach as in Ref. [12]. Second, a 2HDM-based baryogenesis scenario is considered, which generates matter and antimatter asymmetry. This model is motivated by the equal amount of matter and antimatter supposedly generated in the early universe [15]. Searches for baryogenesis were conducted at the LHC with several channels, such as $H \to hh$ [16, 17], $H \to WW/ZZ$ [18–23] and $A \to Zh$ [24, 25]. In addition, searches in the $A \to ZH \to 2\ell 2b/2\ell 2\tau$ [26–29] channels were also carried out in the LHC. In the latter case, for a strong first-order phase transition to occur in the early universe, the $m_A > m_H$ is preferred. Therefore, the $A \to ZH \to 4\ell + X$ model is added to this study to explore regions with jet activities where X could be two leptons, two jets or a pair of SM neutrinos. In this signal, A is a CP-odd scalar which decays to a CP-even scalar H and Z boson. Two decay possibilities are considered for the associated Z and H bosons: $A \to Z(\to \ell^{+}\ell^{-}/j\bar{j}/\nu\bar{\nu})H(\to 4\ell)$ and $A \to Z(\to 2\ell)H(\to 2\ell + j\bar{j}/\nu\bar{\nu})$, which are combined in one signal called $A \to ZH \to 4\ell + X$ signal. In this analysis, only gluon–gluon fusion production mode is considered for both $R \to SH \to 4\ell + E_{\mathrm{T}}^{\mathrm{miss}}$ and $A \to ZH \to 4\ell + X$ signals, as illustrated by Feynman diagrams in Figure. 1.

This paper is organised as follows. The ATLAS experiment is shortly described in Section 2. Section 3 describes the data and Monte Carlo samples, followed by the object reconstruction in Section 4. Section 5 describes the analysis strategy, and the signal and background modelling are discussed in Section 6. Section 7 demonstrates the experimental and theoretical systematic uncertainties. The results are discussed in Section 9, and the conclusion is given in Section 10.

2 ATLAS detector

The ATLAS detector is a multipurpose particle physics detector at the LHC with cylindrical geometry[1] and forward-backwards symmetry [30]. It contains an inner tracker detector (ID) covered by a superconducting solenoid feeding a 2 T magnetic field, electromagnetic (EM) and hadronic calorimeters, and a muon spectrometer with superconducting magnets. The ID has a silicon pixel, a silicon microstrip tracker, a transition radiation tracker, and an insertable B-layer [31] covering the region $|\eta| < 2.5$. The calorimeter design includes lead/liquid-argon, steel/scintillator-tile, copper/liquid-argon, or tungsten/liquid-argon as the absorber fabric. It provides a pseudorapidity coverage of $|\eta| < 4.9$. The muon spectrometer (MS) incorporates superconducting toroidal air-core magnets around the calorimeters, which supply muon identification and momentum measurement for $|\eta| < 2.7$. A trigger system is employed at two stages to select events with an average rate of about 1 kHz for offline analysis [32].

3 Data and simulated event samples

The data used in this analysis consists of proton-proton collisions at a centre-of-mass energy of 13 GeV recorded by the ATLAS detector at the LHC from 2015 to 2018. Events are required to satisfy the data quality requirements to ensure the quality of the collected data [33–35]. After applying the event cleaning criteria, the total integrated luminosity of the entire data reached 139 fb^{-1}.

Simulated events are employed to evaluate the acceptance of the signal and certain background contributions. Each Monte Carlo (MC) event generator produced events that underwent ATLAS detector simulation [36] within the GEANT44 framework [37]. Moreover, the simulated signal and background events received additional inelastic proton-proton interactions. For generating pile-up, PYTHIA8.186 [38] with the A2 set of tuned parameters [39] and the MSTW2008LO [40] parton distribution function (PDF) set was employed as the MC event generator. The simulated events are adjusted through pile-up re-weighting to match the mean number of interactions per bunch crossing observed in the data.

According to ATLAS detector configurations, background and signal events were simulated using MC generators. These events were used for signal optimisation, background parametrisation, and estimation of systematic uncertainties. The $q\overline{q} \to ZZ$ background was generated using SHERPA v2.2.2 [41] with NNPDF 30 NNLO PDF set [42]. The generation was achieved with next-to-leading order (NLO) in the matrix element calculation for 0- and 1-jet final states and leading order (LO) for 2- and 3-jet final states. The accuracy was calculated with the COMIX [43] and OPENLOOPS [44–46]. The SHERPA parton shower [47] for the merging was performed by MEPS@NLO prescription [48]. Electroweak (EW) correction at NLO as a function of the ZZ invariant mass was applied [49, 50]. Similarly, the $gg \to ZZ$ process was simulated by SHERPA v2.2.2 and OPENLOOPS generators. Matrix elements for 0- and 1-jet at LO were calculated and merged with the SHERPA parton shower. The PDF set NNPDF 30 NNLO was used in the generation. The VVV background events, including processes such as ZZZ, ZZW, and $WWWZ$ with at least four prompt charged leptons, were simulated using SHERPA v2.2.2 with NNPDF 30 NNLO PDF set. The

[1] ATLAS uses a right-handed coordinate system with its origin at the nominal interaction point (IP) in the centre of the detector and the z-axis along the beam pipe. The x-axis points from the IP to the centre of the LHC ring, and the y-axis points upwards. Cylindrical coordinates (r, ϕ) are used in the transverse plane, ϕ being the azimuthal angle around the z-axis. The rapidity is defined as $y = (1/2)\ln[(E + p_z)/(E - p_z)]$, where E is the energy and p_z is the longitudinal component of the momentum along the beam pipe. The polar angle θ as $\eta = -\ln\tan(\theta/2)$ defines the pseudorapidity. Angular distance is measured in units of $\Delta R \equiv \sqrt{(\Delta\eta)^2 + (\Delta\phi)^2}$.

Process	Generator and Parton shower	QCD accuracy	Tune and PDF
$R \to SH \to 4\ell + E_{\mathrm{T}}^{\mathrm{miss}}$	Pythia8 [52]	LO	A14 NNPDF 23 LO [54, 55]
$A \to Z(\to X)H(\to 4\ell)$	MadGraph5+Pythia8 [51, 52]	LO	A14 NNPDF 23 LO [54, 55]
$A \to Z(\to 2\ell)H(\to 2\ell + X)$	MadGraph5+Pythia8 [51, 52]	LO	A14 NNPDF 23 LO [54, 55]
$q\bar{q} \to ZZ$	Sherpa+MePs [43, 48, 57, 58]	NLO (0- and 1-jet), LO (2- and 3-jet)	NNPDF 30 NNLO [42]
$gg \to ZZ$	Sherpa+OpenLoops [46, 57, 59, 60]	LO (0- and 1-jet)	NNPDF 30 NNLO [42]
$q\bar{q} \to ZZ$ (EW)	Sherpa [43, 57, 58]	LO	NNPDF 30 NNLO [42]
$ZZZ(4\ell 2\nu, 6\ell 0\nu)$	Sherpa [43, 57, 58]	NNLO	NNPDF 30 NNLO [42]
$WZZ(5\ell 1\nu)$	Sherpa [43, 57, 58]	NNLO	NNPDF 30 NNLO [42]
$WWZ(4\ell 2\nu)$	Sherpa [43, 57, 58]	NNLO	NNPDF 30 NNLO [42]
$t\bar{t}V$ ($V = W/Z$)	MadGraph5+Pythia8 [51, 52]	LO	A14 NNPDF 23 LO [54, 55]
$t\bar{t}$	Powheg-Box+Pythia8 [52, 53]	NNLO+NNLO	A14 NNPDF 23 LO [54, 55]
$WZ \to 3\ell 1\nu$	Powheg-Box+Pythia8 [52, 53]	NNLO	CT10NLO, AZNLOCTEQ6L1 [42]
Z+jets	Sherpa+Comix+OpenLoops+MePs [43, 57, 58]	NLO (0- and 2-jet), LO (3- and 4-jet)	NNPDF 30 NNLO [42]

Table 1: Table summarising the event generators utilized for the simulated signal and background samples, including each process's matrix element and parton distribution function (PDF). Additionally, the table lists the set of tuned parameters used.

$q\bar{q} \to ZZ$ (EW) events, consisting of leptons and two jets, were simulated using Sherpa v2.2.2 with NNPDF 30 NNLO PDF set. Events containing four prompt charged leptons coming from $t\bar{t}V$ backgrounds ($V = Z$ or $W^{\pm}$) were modelled by MadGraph5_aMC@NLO [51] interfaced with Pythia8 [52] for the hadronisation. The $t\bar{t}$ events were generated using Powheg-Box v2 [53] with NNPDF 30 NNLO PDF set. Pythia8 was used as an interface for the showering and hadronisation with the A14 NNPDF23LO tune [54, 55], and EvtGen was used to simulate B-hadron decays. Powheg-Box v2 and Pythia8 were used for the generation and hadronisation of the WZ process, respectively. The Z+jets events were modelled using Sherpa v2.2.0 generator. Matrix elements for 0- and 2-jet at NLO and 3- and 4-jet at LO were calculated with Comix and OpenLoops. The Sherpa parton shower MePs@NLO prescription was used for the merging.

The $R \to SH \to 4\ell + E_{\mathrm{T}}^{\mathrm{miss}}$ signal was simulated using Pythia8 with the A14 tune and NNPDF 23 LO PDF set. For the $A \to Z(\to X)H(\to 4\ell)$ and $A \to Z(\to 2\ell)H(\to 2\ell + X)$ signals, MadGraph5_aMC@NLO was used with the A14 tune and NNPDF 23 LO PDF set. For the $A \to Z(\to X)H(\to 4\ell)$ signal, X is considered to be everything ($j\bar{j}/\ell\ell/\nu\bar{\nu}$), while X is everything except the 2ℓ in the $A \to Z(\to 2\ell)H(\to 2\ell + X)$ signal. The considered R mass is in the range of 390–1300 GeV, with the S mass fixed at 160 GeV, and the A mass is in the range of 320–1300 GeV. The H mass for both signal models is in the range of 220–1000 GeV. Signals were generated using the narrow-width approximation (NWA) [56] in R and H widths for the $R \to SH \to 4\ell + E_{\mathrm{T}}^{\mathrm{miss}}$ signal and in A and H widths for the $A \to ZH \to 4\ell + X$ signal. In the NWA, the A and H bosons are assumed to have negligible natural widths. Several signal mass points were generated using the Large-width approximation (LWA) to test the case where the natural widths are not negligible. Table 1 summarise the generators, parton shower, matrix element, tune, and PDF sets used in signal and background simulation.

4 Object and event selection

4.1 Object reconstruction

The event selection relies on reconstructing and identifying electrons, muons, and jets. The electron energy measurement is improved using a dynamic, topological calorimeter-cell clustering-based method.

This method is particularly effective in cases where an electron radiates a bremsstrahlung photon. More information about this technique can be found in Ref. [61]. Electron candidates are identified as clusters of energy depositions in the calorimeter associated with ID tracks. The final track-cluster matching uses a Gaussian-sum filter (GSF) [62], accounting for bremsstrahlung energy losses. The electron's transverse momentum is calculated from the cluster energy and the track direction at the interaction point. The rejection of background noise depends on the longitudinal and transverse shapes of the electromagnetic showers in the calorimeters, track-cluster matching, and properties of tracks in the ID. All this information, except for that related to track hits, is used to create a likelihood discriminant. The selection criteria combine the likelihood with the number of track hits and define several working points (WP). Electrons with $p_{\mathrm{T}} > 4.5$ GeV and $|\eta| < 2.47$ are selected. A "loose" WP with a 90% efficiency for electrons with $p_{\mathrm{T}} > 30$ GeV is also employed [63].

Muon reconstruction involves matching the track in the MS to the ID [64]. If a complete track is present in both detectors, a global fit is used to perform the matching. Suppose hit information is only available from one of the detectors. In that case, the momentum is determined from the detector with hit information and the track segment from the other detector is used for identification. This method, known as segment-tagged muon, is used only in the central region of the barrel ($|\eta| < 0.1$), where the MS geometrical coverage is reduced. For an ID track with $p_{\mathrm{T}} > 15$ GeV, energy deposition in the calorimeter consistent with a minimum-ionizing particle is used to identify it as a muon (calorimeter-tagged muon). However, it is limited or no ID coverage in the forward region ($2.5 < |\eta| < 2.7$), and the MS track can be used for stand-alone muon identification or in combination with silicon hits if present in the forward ID (combined muon). To achieve good track reconstruction, ID tracks associated with muons must have a minimum number of associated hits in each ID sub-detector. Muons must have a minimum p_{T} of 5 GeV and a maximum η of 2.7. Stand-alone muon candidates which traverse the MS must have hits in all three MS. This analysis uses a "loose" muon identification WP that uses all muon types with an efficiency of 98.5% [64].

The reconstruction of jets applies a particle-flow algorithm [65], which combines measurements from the tracker and the calorimeter. The first step in jet reconstruction is to remove the energy deposited in the calorimeter by all charged particles. Then, the remaining calorimeter energy and tracks matched to the hard interaction are used to create particle-flow objects for the jet reconstruction. The charged-hadron measurement accuracy is enhanced while preserving the calorimeter measurements of neutral-particle energies, leading to an overall improvement. When compared to the usage of the topological clusters algorithm [66], the transverse momentum resolution of jets reconstructed using the particle-flow algorithm at a p_{T} of approximately 30 GeV is about 10% better. The two algorithms exhibit comparable resolutions for p_{T} values above 100 GeV. The anti-k_t algorithm uses a radius parameter $\Delta R = 0.4$ to reconstruct particle-flow jets [67]. After the jets are reconstructed, the jet four-momentum is recalibrated to the EM scale to remove the pile-up effect [68]. To further reduce the impact of pile-up jets, the jet-vertex-tagger (JVT) is used to select jets with $20 < p_{\mathrm{T}} < 60$ GeV and $|\eta| < 2.4$. JVT uses a discriminant based on the projection of the missing transverse momentum from pile-up jets in the central region onto the forward jet [69, 70]. Selected events must have at least one vertex with two associated tracks with $p_{\mathrm{T}} > 500$ MeV, and the primary vertex is chosen to be the vertex with the largest $\sum p_{\mathrm{T}}^2$. The used jets must be in the detector's central region within $|\eta| < 2.5$ with $p_{\mathrm{T}} > 30$ GeV.

Events containing b-hadrons (b-jets) are identified using a multivariate tagging algorithm (b-tagging)[71, 72]. This algorithm utilizes track impact parameters and reconstructed secondary vertices to determine the likelihood that a jet originates from b-quark hadronisation. For jets with $|\eta| < 2.5$, the b-tagging algorithm output is used to select jets that meet the criterion for being b-jets. This criterion has an average efficiency

of 77% for jets from b-quarks in simulated $t\bar{t}$-events with a rejection factor for light-flavour jets of around 30 [71].

After object reconstruction, an overlap-removal procedure is applied to all selected objects to remove ambiguities resulting from objects being reconstructed by several algorithms. The overlapping of objects is resolved by following the recommendations in Ref. [73]. As the same detector information can be used to reconstruct lepton and jet candidates, a procedure is applied to resolve the overlap ambiguities. The muon is selected when an electron and a muon share the same ID track. Unless the muon is calorimeter-tagged and is missing an MS track, the electron is selected. Reconstructed jets which overlap with electrons (muons) in a cone of size $\Delta R = \sqrt{(\Delta\eta)^2 + (\Delta\phi)^2} = 0.2\ (0.1)$ are removed.

The magnitude of the missing transverse momentum is denoted by $E_{\mathrm{T}}^{\mathrm{miss}}$ and is calculated as the negative sum of the transverse momenta of calibrated leptons and jets. Also, a soft term is included in the calculation, which is constructed from all tracks originating from the primary vertex but not associated with any identified lepton or jet [74, 75].

4.2 Event selection

This analysis classifies events into three channels based on the flavours of the selected four leptons: 4μ, $4e$, and $2\mu 2e$. These channels are assigned based on the triggers activated in the event, which include single-lepton, dilepton, and trilepton triggers, with electron(s)-muon(s) triggers included in the latter two. The p_{T} thresholds of the triggers increase slightly during the data-taking period due to the rising luminosity [76, 77]. The p_{T} threshold increased from 20 to 26 GeV and 24 to 26 GeV for single-muon and single-electron triggers, respectively. Although the trigger thresholds varied between 2015 and 2017, their overall efficiency was roughly 98%.

The possible quadruplets in each channel of an event are created by up two lepton pairs with opposite signs and the same flavour (SFOS). The p_{T} for each of the three leading leptons in the quadruplet should be greater than the subsequent ones as 20 GeV, 15 GeV and 10 GeV. The leading and the sub-leading lepton pairs in the quadruplet should have an invariant mass closest and second closest to the Z boson mass. The invariant mass of the leading and sub-leading lepton pairs are m_{Z_1} and m_{Z_2}, respectively. In the selected quadruplet, m_{Z_1} must be within the 50 GeV $< m_{Z_1} <$ 106 GeV range, while m_{Z_2} must be within the 50 GeV $< m_{Z_2} <$ 115 GeV. The selected quadruplets must have their leptons pairs isolated from each other by $\Delta R > 0.1$. If any two SFOS leptons are detected with $m_{\ell\ell}$ below 5 GeV for 4μ and $4e$ quadruplets, the quadruplet is excluded to suppress the contamination from J/ψ mesons. In this analysis, the $Z + \Upsilon$ background contribution is negligible. If, at this point, several quadruplets of different channels are selected, only the quadruplet of the channel with the highest expected signal rate is retained in the order: 4μ, $2e2\mu$, $4e$.

SM Backgrounds, such as the Z+jets and $t\bar{t}$ processes, are suppressed using impact-parameter and track- and calorimeter-based isolation requirements. The transverse impact-parameter significance is the impact parameter calculated with respect to the measured beamline position in the transverse plane divided by its uncertainty, $|d_0|/\sigma d_0$. This significance is required to be less than 3 for muons and 5 for electrons. Additionally, all leptons are required to be associated with the same originating vertex. These requirements help to ensure that leptons originate in hard interaction from a single object. Leptons must be isolated using both track-based and calorimeter-based discriminant. The track-based discriminant takes into account the scalar p_{T} sum of all tracks in the width cone $\Delta R = 0.3$ for muons and 0.2 for electrons (excluding the lepton itself). The ratio of this sum to the lepton p_{T} is expected to be less than 0.15. The pile-up contributions are

suppressed by requiring the cone tracks to originate from the primary vertex. To retain efficiency at higher p_{T}, the size of the track-isolation cone is reduced to 10 GeV/p_{T} for p_{T} above 33 GeV for muons and 50 GeV for electrons.

Since the leptons must originate from a common vertex, the vertexing algorithm [78] is used to fit the ID tracks of the 4l candidates under the assumption that they emanate from a common vertex. The resulting fit quality, represented by the χ^2/ndof value, provides good discrimination between signal and background. For the 4μ channel, a cut of $\chi^2/\mathrm{ndof} < 9$ is applied, while a loose cut of $\chi^2/\mathrm{ndof} < 6$ is used for the other channels. This maintains a signal efficiency greater than 99% for all channels.

The resolution of the four leptons invariant mass system can be improved using a technique to recover the radiative photon production in the Z boson decay (final-state-radiation (FSR)) and a technique to apply constraints on the Z boson mass. In this analysis, the same methodology presented in Ref [79–81] for the $H \to ZZ$ analysis was used to account for FSR photons in the reconstruction of Z bosons, and applying constraints on the Z boson mass. The Z-mass constraint is applied to both Z candidates and improves the resolution of $m_{4\ell}$ by around 15%. This analysis employs the combined 4μ, $4e$, and $2\mu 2e$ channels, collectively called 4ℓ, to account for the limited statistics.

5 Analysis strategy

Section 4.2 covers the selection procedures for the four-lepton quadruplets. In this section, we focus on developing signal regions where the invariant mass of the four leptons is above 200 GeV. The main source of background in this kinematic region is the leptonic decay of the Z boson. Among the various background processes, quark-antiquark annihilation ($q\overline{q} \to ZZ$) is the most significant, contributing to 84.6% of the expected background, while gluon-initiated production ($gg \to ZZ$) accounts for approximately 11.7%. Other SM backgrounds, such as $t\bar{t}V$, Z+jets, $t\bar{t}$, WZ, and VVV, account for about 2.6% of the total background events. These numbers were estimated from MC simulation. However, this study modelled the SM backgrounds using an analytical function, illustrated in Section 6, after the signal regions discussed below.

A cut-based optimisation was used to increase the sensitivity of the $R \to SH \to 4\ell + E_{\mathrm{T}}^{\mathrm{miss}}$ and $A \to ZH \to 4\ell + X$ signals. This involves setting thresholds on various kinematic and topological variables, such as the number of jets (n_{jets}) and b-jets ($n_{b\text{-jets}}$), the invariant mass of the two leading jets (m_{jj}), the momentum of the four-lepton system ($p_{\mathrm{T}}^{4\ell}$), and the $E_{\mathrm{T}}^{\mathrm{miss}}$ significance $\left(E_{\mathrm{T}}^{\mathrm{miss}}/\sqrt{\sum E_{\mathrm{T}}}\right)$. The aim is to separate signal events from background events and maximize the expected significance of the signals. To suppress top-related backgrounds such as $t\bar{t}$ and $t\bar{t}V$, events containing b-jets are vetoed. The remaining events are divided into two groups based on the number of jets: those with no jets ($n_{\mathrm{jets}} = 0$) and those with at least one jet ($n_{\mathrm{jets}} \geq 1$). A two-dimensional scan is applied twice to each group using the $p_{\mathrm{T}}^{4\ell}$ and $E_{\mathrm{T}}^{\mathrm{miss}}$ significance. The first scan determines the optimal threshold for the variables, and the second scan finds other optimal thresholds below the first ones. This process results in specific requirements on the variables that define the signal regions (SRs). The SR requirements depend on the number of jets and b-jets in the event. For events with no jets and no b-jets, $p_{\mathrm{T}}^{4\ell}$ must be greater than 20 GeV, and the $E_{\mathrm{T}}^{\mathrm{miss}}$ significance must be greater than 2. For events with at least one jet but no b-jets, $p_{\mathrm{T}}^{4\ell}$ must be greater than 10 GeV, and the $E_{\mathrm{T}}^{\mathrm{miss}}$ significance must be greater than 3.5. For events with at least one b-jet but no other jets for the scan below the previous thresholds, the $E_{\mathrm{T}}^{\mathrm{miss}}$ significance must be greater than 2.5. Therefore, events in the SR are required to satisfy the following requirements:

Signal region name	$R \to SH \to 4\ell + E_{\mathrm{T}}^{\mathrm{miss}}$	$A \to ZH \to 4\ell + X$
SR1	$n_{b\text{-jets}} = 0$, $n_{\mathrm{jets}} = 0$, $p_{\mathrm{T}}^{4\ell} > 20$ GeV, $E_{\mathrm{T}}^{\mathrm{miss}}$ significance > 2.0	
SR2	$n_{b\text{-jets}} = 0$, $n_{\mathrm{jets}} \geq 1$, $p_{\mathrm{T}}^{4\ell} > 10$ GeV, $E_{\mathrm{T}}^{\mathrm{miss}}$ significance > 3.5	
SR3	$n_{b\text{-jets}} = 0$, $n_{\mathrm{jets}} \geq 1$, $p_{\mathrm{T}}^{4\ell} > 0$ GeV, $E_{\mathrm{T}}^{\mathrm{miss}}$ significance > 2.5	
SR4	–	$n_{b\text{-jets}} \geq 1$
SR5	–	$n_{b\text{-jets}} = 0$, $n_{\mathrm{jets}} \geq 2$, $\lvert m_{jj} - m_Z \rvert < 20$ GeV
SR6	–	$n_{b\text{-jets}} = 0$, $n_{\mathrm{jets}} \geq 2$, $\lvert m_{jj} - m_Z \rvert > 20$ GeV
SR7	–	$n_{b\text{-jets}} = 0$, $n_{\mathrm{jets}} = 1$

Table 2: Table summarising the requirements of the signal regions (SRs) selection for the $R \to SH \to 4\ell + E_{\mathrm{T}}^{\mathrm{miss}}$ and $A \to ZH \to 4\ell + X$ signals for $m_{4\ell} > 200$ GeV.

- $n_{b\text{-jets}} = 0$ and $n_{\mathrm{jets}} = 0$ with $p_{\mathrm{T}}^{4\ell} > 20$ GeV and $E_{\mathrm{T}}^{\mathrm{miss}}$ significance > 2.0 (SR1)
- $n_{b\text{-jets}} = 0$ and $n_{\mathrm{jets}} \geq 1$ with $p_{\mathrm{T}}^{4\ell} > 10$ GeV and $E_{\mathrm{T}}^{\mathrm{miss}}$ significance > 3.5 (SR2)
- $n_{b\text{-jets}} = 0$ and $n_{\mathrm{jets}} \geq 1$ with $p_{\mathrm{T}}^{4\ell} > 0$ GeV and $E_{\mathrm{T}}^{\mathrm{miss}}$ significance > 2.5 (SR3)

The SRs mentioned earlier are used for both $R \to SH \to 4\ell + E_{\mathrm{T}}^{\mathrm{miss}}$ and $A \to ZH \to 4\ell + X$ models. However, since the $A \to ZH \to 4\ell + X$ signal involves more jet activities, additional four-jet categories are defined as follows:

- Since we selected events with no b-jets on the previous categorisations, we require events with at least one b-jets ($n_{b\text{-jets}} \geq 1$) to account for the events containing b-jets (SR4).
- There are events not selected with SR2 and SR3. Therefore, signal region five (SR5) requires events with no b-jets, and at least two jets with $n_{\mathrm{jets}} \geq 2$ and $\lvert m_{jj} - m_Z \rvert < 20$ GeV.
- Events with no b-jets and at least two jets which fall within $\lvert m_{jj} - m_Z \rvert > 20$ GeV are put into signal region six (SR6).
- Signal region seven (SR7) contains events with no b-jets and exactly one jet.

A few events with no b-jets and jets left out of SR1 are not considered. Three SRs were defined for the $R \to SH \to 4\ell + E_{\mathrm{T}}^{\mathrm{miss}}$ signal, while seven SRs were defined for the $A \to ZH \to 4\ell + X$ signal as summarised in Table 2. Figure 7 in Appendix A shows a flowchart of SRs.

6 Signal and background modelling

MC simulation is used to parameterise the constructed four leptons invariant mass ($m_{4\ell}$) distribution for the SM backgrounds. Meanwhile, the signal shape is taken directly from the MC simulation, as illustrated below.

6.1 Signal model

A few mass points are generated for $R \to SH \to 4\ell + E_{\mathrm{T}}^{\mathrm{miss}}$ and $A \to ZH \to 4\ell + X$ signals, as demonstrated in Section 3. To cover a broader mass spectrum, a linear interpolation method described in Ref. [82] is used to get signal shapes between the generated masses in either of the (m_R, m_H) or (m_A, m_H) planes. Because the signal depends on the A and H masses, interpolating the signal must be done in two steps. The first step is to fix the H mass and interpolate the $m_A - m_H$ or the A mass. The interpolated signals along the A mass are input for a second interpolation step where the A mass is fixed, and 10 GeV varies the H mass. The same interpolating procedures are used for the $R \to SH \to 4\ell + E_{\mathrm{T}}^{\mathrm{miss}}$ signal to get the mass points between the generated samples.

To ensure that the interpolation works well, a known histogram from the MC simulation is used as a benchmark for the comparison. For instance, parameter-ordered histograms such as $(m_A, m_H) = (510, 220)$ GeV, $(m_A, m_H) = (540, 250)$ GeV, and $(m_A, m_H) = (590, 300)$ GeV, one can compare the interpolation between $(m_A, m_H) = (510, 220)$ GeV and $(m_A, m_H) = (590, 300)$ GeV at the parameter value corresponding to $(m_A, m_H) = (540, 250)$ GeV. This helps to verify the accuracy of the interpolation, as shown in Figure 2(a) for $A \to Z(\to j\bar{j}/\ell^+\ell^-/\nu\bar{\nu})H(\to 4\ell)$ signal, and Figure 2(b) for the $A \to Z(\to \ell^+\ell^-)H(\to 2\ell + j\bar{j}/\nu\bar{\nu})$ signal. Notice that the $m_A - m_H$, in this case, is equal for all the mass points used in the interpolations. Similarly, Figure 2(c) shows the interpolating $(m_R, m_H) = (420, 250)$ GeV mass point from $(m_R, m_H) = (390, 220)$ GeV and $(m_R, m_H) = (470, 300)$ GeV mass points. Several samples were compared, and the systematic uncertainty, taken as the difference between the interpolated and simulated signal distributions, was found to have a negligible impact on the limit and was therefore omitted.

6.2 Background model

The $m_{4\ell}$ shape of the backgrounds is obtained from MC simulation using a parameterised empirical function to decrease statistical uncertainties originating from the limited number of simulated events. Four background templates are used: $q\bar{q} \to ZZ$, $gg \to ZZ$, VVV, and others. The VVV has a different shape from the rest of the backgrounds, so it is kept on a different template. Backgrounds such as $q\bar{q} \to ZZ$ (EW), $t\bar{t}V$, $t\bar{t}$, Z+jets and WZ are combined in a template called others. Each of the background templates is fitted with an analytical function for $m_{4\ell}$ between 200–1200 GeV, as follows:

$$f(m_{4\ell}) = H(m_0 - m_{4\ell})\, f_1(m_{4\ell})\, C_1 + H(m_{4\ell} - m_0)\, f_2(m_{4\ell})\, C_2, \tag{1}$$

where:

$$f_1(m_{4\ell}) = \frac{a_1 \cdot m_{4\ell} + a_2 \cdot m_{4\ell}^2}{1 + \exp\left(\frac{m_{4\ell} - a_1}{a_3}\right)} \tag{2}$$

$$f_2(m_{4\ell}) = \left(1 - \frac{m_{4\ell}}{n_C}\right)^{b_1} \cdot \left(\frac{m_{4\ell}}{n_C}\right)^{\left(b_2 + b_3 \cdot \ln\left(\frac{m_{4\ell}}{n_C}\right)\right)} \tag{3}$$

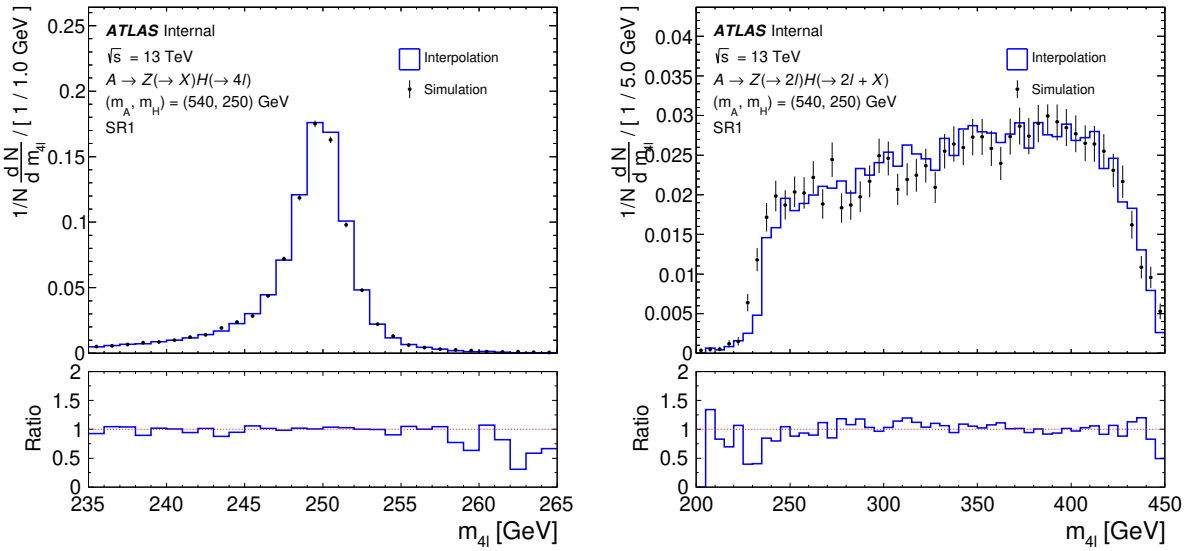

(a) (b)

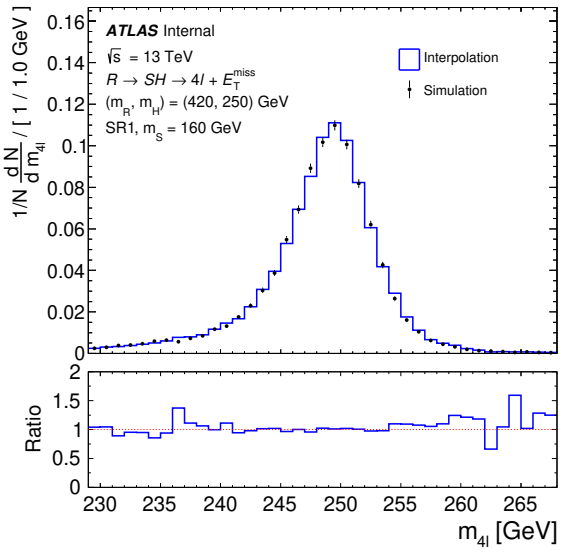

(c)

Figure 2: The $m_{4\ell}$ distributions of the interpolated (blue) and MC simulated (black-filled data point) signals for (a) $A \to Z(\to j\bar{j}/\ell^+\ell^-/\nu\bar{\nu})H(\to 4\ell)$ and (b) $A \to Z(\to \ell^+\ell^-)H(\to 2\ell + j\bar{j}/\nu\bar{\nu})$ signals with $(m_A, m_H) = (540, 250)$ GeV mass point and (c) the $R \to SH \to 4\ell + E_{\mathrm{T}}^{\mathrm{miss}}$ signal with $(m_R, m_H) = (420, 250)$ GeV and $m_S = 160$ GeV mass point. The lower panel represents the ratio between the interpolated and MC-simulated histograms.

$$C_1 = \frac{1}{f_1(m_0)}, \qquad C_2 = \frac{1}{f_2(m_0)}$$

f_1 models the ZZ threshold around $2 \cdot m_Z$, and f_2 describes the high mass tail. The transition between f_1 and f_2 functions is performed by the Heaviside step function $H(x)$ around m_0, where m_0 is fixed to 260, 240, 250 and 230 for the $q\overline{q} \to ZZ$, $gg \to ZZ$, VVV, and others backgrounds, respectively. The transition point is determined by optimising the function's smoothness. A constant $n_C = 13$ TeV scales the $m_{4\ell}$ in the high mass region. C_1 and C_2 ensure the continuity of the function around the m_0 corresponding to f_1 and f_2. Overall, a good fit quality was acquired with the empirical function in all SRs. The integral error calculated from the fit function is considered a source of systematic uncertainty and is treated as a nuisance parameter during the final fit.

7 Systematic uncertainties

This section discusses the sources of systematic uncertainties considered in this analysis, including experimental and theoretical uncertainties for the signal and background processes. Statistical uncertainties arising from the MC event generation limitations are also considered. Additionally, uncertainties introduced by the background parameterisation are considered a source of uncertainty and propagated to the final fit. Each systematic component is treated as a nuisance parameter and profiled into the fit results. The systematic uncertainties are evaluated using the invariant mass of the four leptons system as a discriminant.

7.1 Experimental uncertainties

Experimental uncertainties, such as object reconstruction and identification, trigger efficiencies, energy scale, and resolution, are calculated for signal and background processes. The systematic experimental uncertainties are evaluated by computing the ratio between the integral of the $m_{4\ell}$ distribution with the interested nuisance parameter weight modified by one standard deviation and the integral of the $m_{4\ell}$ distribution using the nominal weight. The results are expressed as percentages for nuisance parameters with upward and downward variations corresponding to $\pm 1\sigma$. Signal samples were divided into three categories depending on the quantity of the energy gap ($m_A - m_H$ or $m_R - m_H$) to simplify estimating the experimental systematic uncertainties for the signals. The gaps include samples with low ($<$ 500 GeV), medium (500 $>$ and $<$ 700 GeV) and high ($>$ 1300 GeV) energy gaps. These ranges are for the $R \to SH \to 4\ell + E_{\mathrm{T}}^{\mathrm{miss}}$ process, and these ranges are slightly different for the $A \to ZH \to 4\ell + X$ process. The systematic uncertainties are evaluated for three signal mass points from each energy gap for both signals. Each result is combined by calculating the mean of the three samples per energy gap.

The uncertainty on the total integrated luminosity of the data recorded between 2015 and 2018 is ±1.7% [83]. In addition, systematic uncertainty introduced by re-scaling the simulated pile-up to the data is considered. The data scale factor is calculated using data to MC comparisons which comes with uncertainty. The current MC's nominal value is 1.0/1.03, scaled upward by 1.0/0.99 and downward by 1.0/1.07 to account for the pile-up re-weighting uncertainty [84]. It is estimated to be up to 2.5% for the $R \to SH \to 4\ell + E_{\mathrm{T}}^{\mathrm{miss}}$ signal, less than 1.0% for the $A \to ZH \to 4\ell + X$ signal and about 3% for the VVV and other backgrounds.

The lepton identification, isolation and reconstruction efficiency, energy/momentum scale, and resolution are derived from data using $J/\psi \to \ell\ell$ and $Z \to \ell\ell$ decay events. The uncertainties in the lepton efficiency

are calculated following the method presented in Refs. [63, 64] for muons and electrons. Generally, their effect on the signal yields is less than 1% for the $R \to SH \to 4\ell + E_{\mathrm{T}}^{\mathrm{miss}}$ signal and up to 4% for the $A \to ZH \to 4\ell + X$ signal. These uncertainties are about 1.5% for the VVV background and roughly 1.7% for the other background. The uncertainties in the jet energy scale and resolution come from sources such as uncertainties in the absolute and relative "in situ" calibration and the correction for pile-up [68]. In total, uncertainties due to the jet energy scale and energy resolution are estimated to be 4.3% for the $R \to SH \to 4\ell + E_{\mathrm{T}}^{\mathrm{miss}}$ signal, 4.7% for the $A \to ZH \to 4\ell + X$ signal, approximately 7% for the VVV background and 10.4% for the other backgrounds. In addition, flavour tagging and jet-vertex-tagger (JVT) uncertainties due to the disagreement in selecting the jet flavour are calculated by altering the uncertainty of the tagged jet flavour efficiency by $\pm 1\sigma$. The total estimated flavour tagging uncertainties are 4.3% for the $R \to SH \to 4\ell + E_{\mathrm{T}}^{\mathrm{miss}}$ and $A \to ZH \to 4\ell + X$ signals, 8.9% for the VVV background and 8.5% for the other backgrounds. The $E_{\mathrm{T}}^{\mathrm{miss}}$ is reconstructed using a signal associated with hard objects—namely muons, electrons, photons, hadronically decaying taus and jets. Objects not related to the hard ones are referred to as soft objects. The $E_{\mathrm{T}}^{\mathrm{miss}}$ uncertainty measurement is considered on the soft track term described in Ref. [85]. Two components were considered—the $E_{\mathrm{T}}^{\mathrm{miss}}$ parallel and perpendicular to hard objects momenta. The overall $E_{\mathrm{T}}^{\mathrm{miss}}$ uncertainty for the $R \to SH \to 4\ell + E_{\mathrm{T}}^{\mathrm{miss}}$ signal and VVV background is less than 1%, about 6% for the $A \to ZH \to 4\ell + X$ signal and 12.6% and 7.8% for the other backgrounds.

7.2 Theoretical uncertainties

This analysis considers the effects of the parton distribution functions (PDFs), high-order QCD correction, initial- and final-state radiation (ISR/FSR), and parton showering (PS) and hadronisation uncertainties. The theoretical scale uncertainties on the signal samples are assessed by varying the factorisation. Renormalisation scales up and down from their nominal values by a factor of two in each category. The scale uncertainty is the largest deviation in each category divided by the inclusive selections.

The PDF uncertainty is estimated using the SysCalc [86] package in conjunction with Madgraph. The uncertainty is determined by considering the envelope of variations among alternative PDFs differ from the internal PDF error sets (NNPDF 3.0 PDF). The calculation follows the PDF4LHC recommendations provided in Ref. [87]. The ISR/FSR, PS and hadronisation uncertainties are evaluated by varying the signal eigen-variables in Pythia and comparing Herwig v7.1.3 [88] with Pythia for the signal samples. The overall theoretical uncertainty for the signal processes is about 1%. The theoretical systematic uncertainties on the SM backgrounds are included as a shape systematic and summarised below.

7.3 Systematic uncertainties on signal and backgrounds shapes

The interpolation procedures introduce uncertainties in the signal shape, which are accounted for using the variation in the signal scale and resolution. These uncertainties are extracted by modifying some double-sided Crystal Ball function parameters as discussed in Section 6.1.

To account for any possible biases introduced by the analytical function discussed in Section 6.2, uncertainties stemming from the background parameterisation are considered. These uncertainties are calculated by evaluating the error in the integral of the fitted function while also taking into account the errors in the parameters resulting from the fit. The errors are estimated using the correlation values obtained from the fit. The effect of uncertainty on the background shape is divided into two regions: 200 GeV $\leq m_{4\ell} \leq$ 700 GeV and 700 GeV $< m_{4\ell} \leq$ 1200 GeV.

PDF and QCD scale uncertainties influence the shape of the $m_{4\ell}$ distribution for $q\overline{q} \to ZZ$ and $gg \to ZZ$ processes are included. The QCD uncertainty is estimated to be up to 10% for $q\overline{q} \to ZZ$ and $gg \to ZZ$ backgrounds. The PDF uncertainty is less the 25% for $q\overline{q} \to ZZ$ and about 30% for the $gg \to ZZ$ background. A high-order electro-weak correction (HOEW) uncertainty on the $m_{4\ell}$ shape is considered for $q\overline{q} \to ZZ$ background, which is estimated to be less than 10%. A few nuisance parameters which affect the shape of the $m_{4\ell}$ distribution of the $q\overline{q} \to ZZ$ and $gg \to ZZ$ background are accounted for in this analysis. The parton-shower uncertainty is evaluated by varying parameters in the parton-shower tunes, such as CKKW and QSF settings, and by different showering options.

8 Statistical procedures

The invariant mass of the four leptons ($m_{4\ell}$) is utilised as a discriminant to examine the null and alternative hypotheses using the profile likelihood ratio technique [89]. The null hypothesis results in smoothed backgrounds that fall from the low mass range to the higher mass range of the $m_{4\ell}$ distribution. In contrast, the alternative hypothesis constructs a signal structure around the H mass. The signal and background contributions in the $m_{4\ell}$ distribution are extracted via binned maximum-likelihood fit by the signal-plus background hypotheses to extract any indications for new physics. The profile likelihood function is defined by the probability of observing n events times the product sum of the weighted signal and background events, as shown below:

$$\mathcal{L}(m^n_{4\ell}|\sigma(gg \to A/R), \vec{\theta}) = \prod_{r=\text{SRs}}^{n_r} \prod_{b=\text{bin}}^{n_b} \text{Poisson}\left(n_{r,b} \mid S_{r,b} + \sum_{B} B_{r,b}(\vec{\theta})\right) \times \prod_{i} G_i(0|\vec{\theta}, 1), \quad (4)$$

where $\sigma(gg \to A/R)$ denotes the signal strength (parameter of interest) for the $A \to ZH \to 4\ell + X$ or $R \to SH \to 4\ell + E_{\text{T}}^{\text{miss}}$ signal, the expected signal and background yields in each $m_{4\ell}$ distribution bin are represented by the S and B, respectively. The expected signal yields S is calculated by:

$$S = \sigma(gg \to A/R) \times \mathcal{B}(A/R \to ZH/SH) \times \mathcal{B}(H \to ZZ) \times \mathcal{B}(ZZZ/ZZ \to 4\ell) \times A \times \int L \, \mathrm{d}t, \quad (5)$$

where A is the acceptance times the efficiency, and $\int L \, \mathrm{d}t = 139$ fb^{-1} is the integrated luminosity of the data. A collection of nuisance parameters is introduced to describe how systematic uncertainties influence the predicted number of signal and background events and the shape of the PDFs. These parameters are constrained to their nominal values within the calculated uncertainties using Gaussian constraints by $G(\vec{\theta})$, in which $\vec{\theta}$ is a vector containing the nuisance parameters. The dependency of the analysis on SRs for each event is indicated in the product by the index "r". In each SR, the normalisation for $q\overline{q} \to ZZ$ and $gg \to ZZ$ processes (ZZ background) are calculated by a likelihood fit to the data. The ZZ background normalisation is denoted by the μ^{ZZ}_{norm} parameter. The benefit of taking the ZZ background normalisation from the data is to reduce the background dependency on the theoretical systematic uncertainties.

	SR1	SR2	SR3	SR4	SR5	SR6	SR7
$q\bar{q} \to ZZ$	132.2 ± 12	17.1 ± 6	42 ± 6.8	39.8 ± 6.5	156.2 ± 12.7	86.3 ± 11.6	549 ± 69.4
$gg \to ZZ$	31.9 ± 5.9	3.2 ± 3.1	8.3 ± 3.1	6.6 ± 2.5	22.1 ± 3.5	9.4 ± 4.5	102.1 ± 71.5
VVV	7.5 ± 0.4	4.8 ± 0.3	1.5 ± 0.2	0.2 ± 0	1.1 ± 0.1	0.5 ± 0.1	1.6 ± 0.1
others	5.5 ± 0.9	7.1 ± 0.8	3.6 ± 0.9	2.5 ± 0.3	17.5 ± 0.9	37.6 ± 2.4	11.3 ± 0.8
μ^{ZZ}_{norm}	1.1 ± 0.1	1.3 ± 0.6	1 ± 0.2	0.9 ± 0.2	0.8 ± 0.1	1.4 ± 0.3	1 ± 0.1
Total background	177.1 ± 13.3	32.2 ± 5.6	55.3 ± 7.4	49 ± 7	196.9 ± 14	133.8 ± 11.6	664 ± 26.3
Observed	177	32	55	49	197	135	664

Table 3: Observed and expected post-fit event yields for $m_{4\ell} > 200$ GeV with their uncertainties. The expected yields and their uncertainties are obtained from a simultaneous fit to data under the background-only hypothesis on all seven signal regions (SRs) discussed in Section 5. The μ^{ZZ}_{norm} is the normalisation factor for $q\bar{q} \to ZZ$ and $gg \to ZZ$ backgrounds which is considered during the fit. The others background include $q\bar{q} \to ZZ$ (EW), $t\bar{t}V$, $t\bar{t}$, Z+jets and WZ processes.

9 Results

Table 3 displays the yields in each of the seven SRs described in Section 5. The observed and expected numbers of events in each SR were obtained using a simulated binned maximum-likelihood fit, assuming the background-only hypothesis. We performed signal-plus-background binned maximum-likelihood fits on the $m_{4\ell}$ distribution to search for potential excesses beyond the expected SM backgrounds. This fit model is based on the statistical framework discussed in Section 8. We scanned the m_R (m_A) range 390–1300 (320–1300) GeV and the m_H range 220–1000 GeV for the $R \to SH \to 4\ell + E_{\text{T}}^{\text{miss}}$ ($A \to ZH \to 4\ell + X$) signal. The fit was performed in steps of 10 GeV, in which 4187 (m_R, m_H) and 4740 (m_A, m_H) mass points in NWA for each SR were tested for the $R \to SH \to 4\ell + E_{\text{T}}^{\text{miss}}$ and $A \to ZH \to 4\ell + X$, respectively. The resulting test statistics were used to construct p-values and significance estimates, which were then used to evaluate the compatibility of the data with the background-only hypothesis and the presence of new physics in the data.

The four leptons invariant mass distribution for the $R \to SH \to 4\ell + E_{\text{T}}^{\text{miss}}$ signal with $(m_R, m_H) = (500, 300)$ GeV mass point in all three SRs are shown in Figure 3. Figures 4 and 5 show the $m_{4\ell}$ distribution in the seven SRs defined for the $A \to ZH \to 4\ell + X$ signal with $(m_A, m_H) = (510, 380)$ GeV mass point. No significant deviation from the SM backgrounds is observed in the data. The p values as a function of the m_R/m_A and m_H are shown in Appendix B. Excesses, around 2.0 standard deviations, for a few mass points are shown in Figure 8(a) for the $R \to SH \to 4\ell + E_{\text{T}}^{\text{miss}}$ signal, and in Figure 8(b) for the $A \to ZH \to 4\ell + X$ signal. The most significant excess comes from the $A \to ZH \to 4\ell + X$ signal at $(m_A, m_H) = (510, 380)$ GeV mass point with a local significance of 2.5 standard deviations. As no significant excess was observed in comparison to the background predictions, the results were translated into upper limits on the production cross-section of the $R \to SH \to 4\ell + E_{\text{T}}^{\text{miss}}$ and $A \to ZH \to 4\ell + X$ signals times the branching fractions. The branching fractions considered are $\mathcal{B}(R \to SH)$, $\mathcal{B}(H \to ZZ)$ and $\mathcal{B}(ZZ \to 4\ell)$ for the $R \to SH \to 4\ell + E_{\text{T}}^{\text{miss}}$ process. For the $A \to ZH \to 4\ell + X$ process, the branching fractions are $\mathcal{B}(A \to ZH)$, $\mathcal{B}(H \to ZZ)$ and $\mathcal{B}(ZZZ \to 4\ell)$.

The CL_s approach in the asymptotic approximation [89, 91] calculates the upper limit at 95% confidence level (CL) on the explored phase space. The upper limit, either on $\sigma(gg \to R) \times \mathcal{B}(R \to SH) \times \mathcal{B}(H \to$

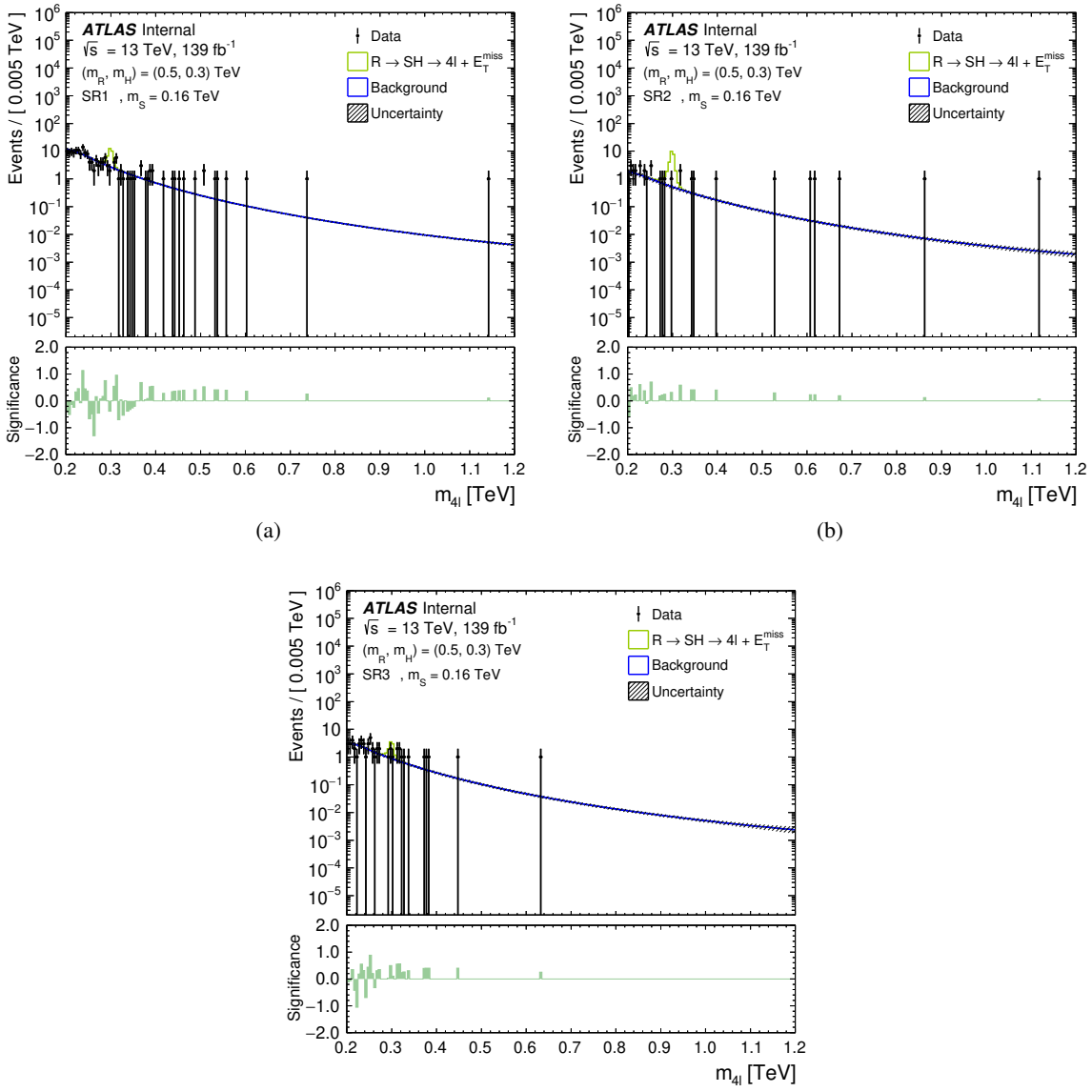

Figure 3: The observed and expected invariant mass of the four leptons system distributions of the $R \to SH \to 4\ell + E_{\mathrm{T}}^{\mathrm{miss}}$ signal with $(m_R, m_H) = (500, 300)$ GeV and $m_S = 160$ GeV for the (a) SR1, (b) SR2 and (c) SR3 under background-only fit to data. The total background (blue) includes $q\bar{q} \to ZZ$, $gg \to ZZ$, $q\bar{q} \to ZZ$ (EW), $t\bar{t}V$, $t\bar{t}$, Z+jets and WZ processes. The distribution of the $(m_A, m_H) = (510, 380)$ GeV signal (green) is normalised to 50 times the observed upper limit (5.7 fb) discussed in Section 9. The hatched lines show the systematic uncertainty of the Monte Carlo prediction, while the error bar on the data denotes the statistical uncertainty. The lower panel displays the significance of each bin, which is determined by the residual of the data corresponding to the fitted background taking the statistical uncertainty of the data into account. The recommended significance formula in Ref. [90] is used in the calculation.

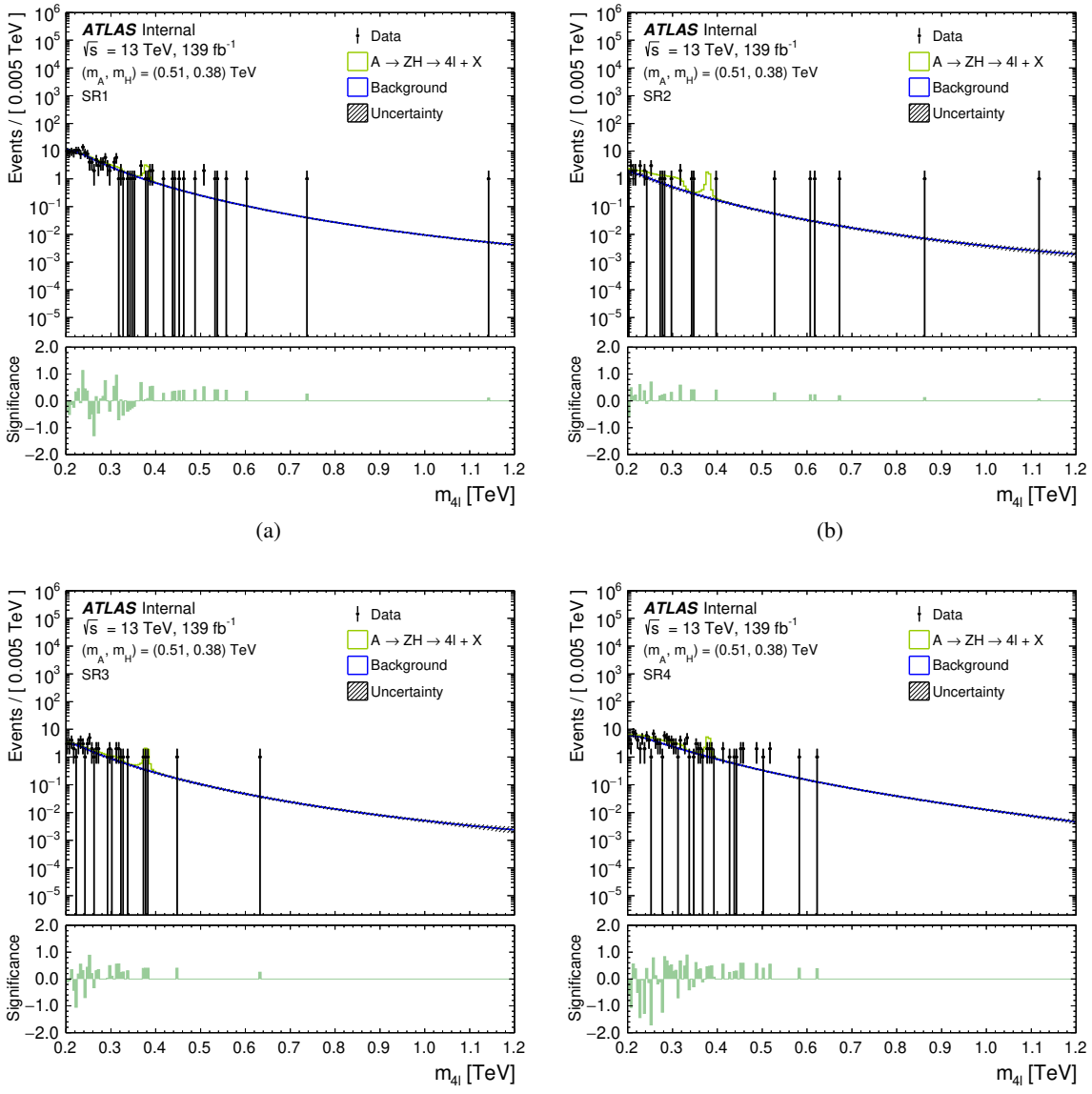

Figure 4: The observed and expected invariant mass of the four leptons system distributions of the $A \to ZH \to 4\ell + X$ signal with $(m_A, m_H) = (510, 380)$ GeV for the (a) SR1, (b) SR2, (c) SR3 and (d) SR4 under background-only fit to data. The total background (blue) includes $q\overline{q} \to ZZ$, $gg \to ZZ$, $q\overline{q} \to ZZ$ (EW), $t\bar{t}V$, $t\bar{t}$, Z+jets and WZ processes. The distribution of the $(m_A, m_H) = (510, 380)$ GeV signal (green) is normalised to 50 times the observed upper limit (18 fb) discussed in Section 9. The hatched lines show the systematic uncertainty of the Monte Carlo prediction, while the error bar on the data denotes the statistical uncertainty. The lower panel displays the significance of each bin, which is determined by the residual of the data corresponding to the fitted background taking the statistical uncertainty of the data into account. The recommended significance formula in Ref. [90] is used in the calculation.

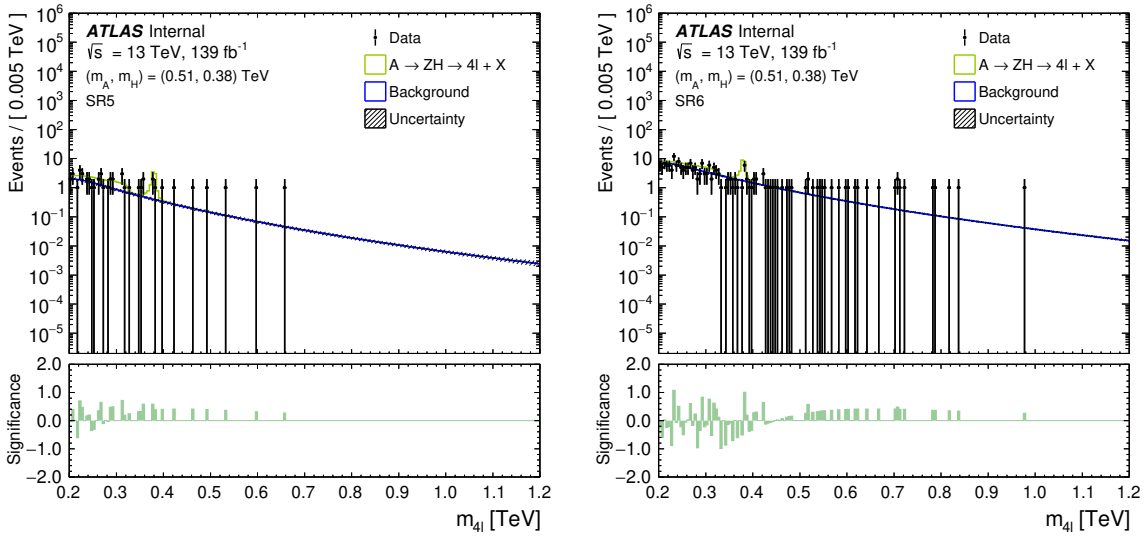

(a)

(b)

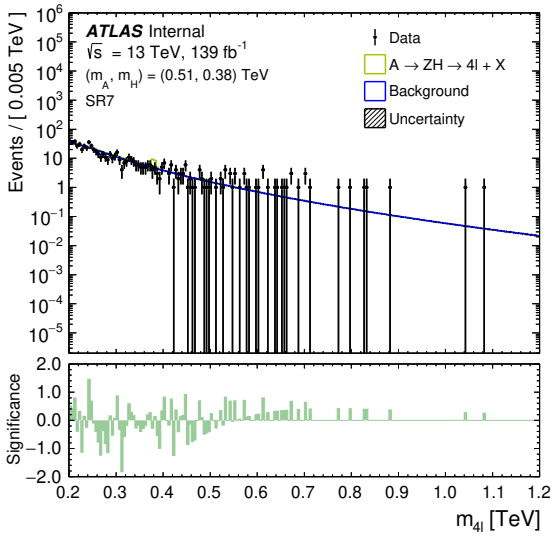

(c)

Figure 5: The observed and expected invariant mass of the four leptons system distributions of the $A \to ZH \to 4\ell + X$ signal with $(m_A, m_H) = (510, 380)$ GeV for the (a) SR5, (b) SR6 and (c) SR7 under background-only fit to data. The total background (blue) includes $q\bar{q} \to ZZ$, $gg \to ZZ$, $q\bar{q} \to ZZ$ (EW), $t\bar{t}V$, $t\bar{t}$, Z+jets and WZ processes. The distribution of the $(m_A, m_H) = (510, 380)$ GeV signal (green) is normalised to 50 times the observed upper limit (18 fb) discussed in Section 9. The hatched lines show the systematic uncertainty of the Monte Carlo prediction, while the error bar on the data denotes the statistical uncertainty. The lower panel displays the significance of each bin, which is determined by the residual of the data corresponding to the fitted background taking the statistical uncertainty of the data into account. The recommended significance formula in Ref. [90] is used in the calculation.

Width assumptions	Mass points [GeV]	Upper limits in the $\sigma(gg \to A)$ [fb]		Fractions
		Observed	Expected	
Narrow width	$(m_A, m_H) = (320, 220)$	0.224	0.280	–
	$(m_A, m_H) = (1190, 600)$	0.061	0.045	–
$(\Gamma_A/m_A, \Gamma_H/m_H) = (15, 5)$	$(m_A, m_H) = (320, 220)$	0.411	0.463	1.7
	$(m_A, m_H) = (1190, 600)$	0.106	0.077	1.7
$(\Gamma_A/m_A, \Gamma_H/m_H) = (30, 10)$	$(m_A, m_H) = (320, 220)$	0.510	0.563	2.0
	$(m_A, m_H) = (1190, 600)$	0.118	0.085	1.8

Table 4: Observed and expected upper limits at 95% confidence level (CL) on the $\sigma(gg \to A) \times \mathcal{B}(A \to ZH) \times \mathcal{B}(H \to ZZ) \times \mathcal{B}(ZZZ \to 4\ell)$ of different large-width approximation (LWA) signals to compare to the narrow-width approximation (NWA) signal. The fraction is the ratio between the expected LWA's upper limit and the expected NWA's upper limit. The Γ_A and Γ_H denote the width of the A and H boson, respectively.

$ZZ) \times \mathcal{B}(ZZ \to 4\ell)$ or on $\sigma(gg \to A) \times \mathcal{B}(A \to ZH) \times \mathcal{B}(H \to ZZ) \times \mathcal{B}(ZZZ \to 4\ell)$, for a specific mass hypothesis is obtained by fixing the H mass parameter to a constant value and optimising the probability function for nuisance parameters. The observed and expected upper limit of NWA R and H bosons for the $R \to SH \to 4\ell + E_{\mathrm{T}}^{\mathrm{miss}}$ signal are shown in Figures 6(a) and 6(b) in the (m_H, m_R) plane where the z-axis displays the $\sigma(gg \to R) \times \mathcal{B}(R \to SH) \times \mathcal{B}(H \to ZZ) \times \mathcal{B}(ZZ \to 4\ell)$ in the unit of fb. The upper limits for $R \to SH \to 4\ell + E_{\mathrm{T}}^{\mathrm{miss}}$ signal range from 0.031 fb for $(m_R, m_H) = (1300, 980)$ GeV to 0.539 fb for $(m_R, m_H) = (410, 240)$ GeV. In contrast, the expected upper limits vary from 0.035 fb to 0.318 fb for the same mass points. Similarly, Figures 6(c) and 6(d) show the observed and expected upper limits for the $A \to ZH \to 4\ell + X$ signal in the (m_H, m_A) plane, in which the z-axis represents the upper limits on the $\sigma(gg \to A) \times \mathcal{B}(A \to ZH) \times \mathcal{B}(H \to ZZ) \times \mathcal{B}(ZZZ \to 4\ell)$. For the $A \to ZH \to 4\ell + X$ signal, the upper limits run from 0.027 fb for $(m_A, m_H) = (1300, 760)$ GeV to 0.419 fb for $(m_A, m_H) = (430, 240)$ GeV, whereas the corresponding expected upper limits range from 0.038 fb to 0.244 fb. The upper limits are also calculated using the toy MCs method to check the asymptotic approach's validity at high H boson mass where the statistic is limited for a few mass points. The observed (expected) upper limits using the asymptotic approach were underestimated by 10% (1%) for the $R \to SH \to 4\ell + E_{\mathrm{T}}^{\mathrm{miss}}$ signal and by 15% (3%) for the $A \to ZH \to 4\ell + X$ signal.

The analysis focused on studying heavy resonances with NWA A or R and H bosons produced via gluon-gluon fusion for $A \to ZH \to 4\ell + X$ and $R \to SH \to 4\ell + E_{\mathrm{T}}^{\mathrm{miss}}$ processes. However, it would be interesting to study the effect of the large-width approximation (LWA) in a similar scenario. Two low and high mass points, $(m_A, m_H) = (320, 220)$ GeV and $(m_A, m_H) = (1190, 600)$ GeV, for the $A \to ZH \to 4\ell + X$ signal were generated using similar configurations as the NWA signal, to give a perspicuity into this. Upper limits are computed for signal assumptions in which the A and H bosons favour a non-negligible natural widths correspondence with the experimental mass resolution. The upper limit decreases as the natural width of the A and H bosons increases, for example, in the case where an $A \to ZH \to 4\ell + X$ signal that produces A and H bosons with natural widths of 15% and 5%, respectively, of their experimental mass resolution, the upper limit declined by a factor of 1.7 correspond to the NWA upper limit for both low and high mass points. In the $(\Gamma_A/m_A, \Gamma_H/m_H) = (30\%, 10\%)$ case, the upper limit is reduced by a factor of 2 for the low mass point and by a factor of 1.8 for the high mass point comparing to the NWA scenario. Table 4 summarises widths assumptions, mass points and upper limits

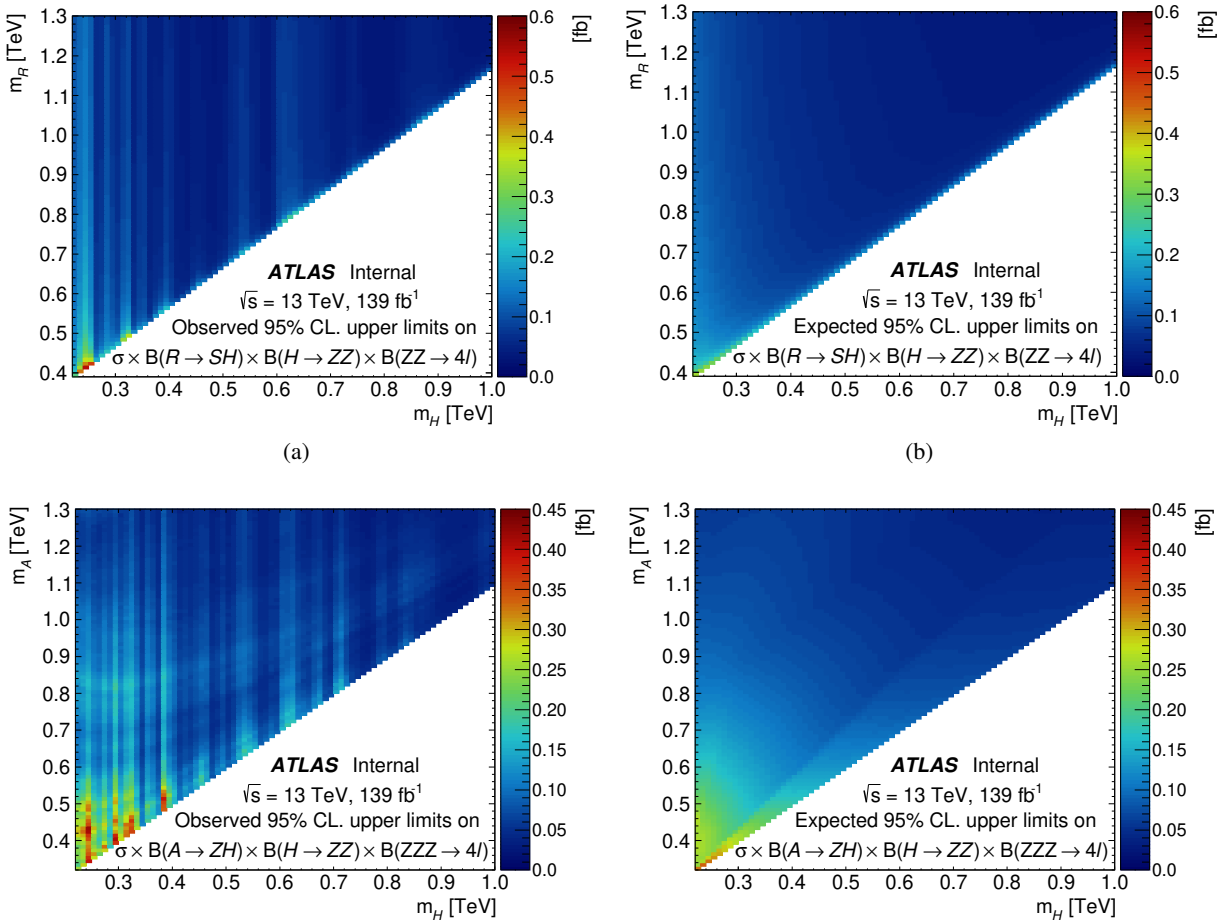

Figure 6: The observed (left) and expected (right) upper limits at 95% confidence level in (a), (b) the $\sigma(gg \to R) \times \mathcal{B}(R \to SH) \times \mathcal{B}(H \to ZZ) \times \mathcal{B}(ZZ \to 4\ell)$ on (m_H, m_R) plane with $m_S = 160$ GeV for the $R \to SH \to 4\ell + E_{\mathrm{T}}^{\mathrm{miss}}$ signal, and in (c), (d) the $\sigma(gg \to A) \times \mathcal{B}(A \to ZH) \times \mathcal{B}(H \to ZZ) \times \mathcal{B}(ZZZ \to 4\ell)$ on (m_H, m_A) plane for the $A \to ZH \to 4\ell + X$ signal.

for LWA and NWA.

10 Conclusion

A search is performed for new heavy resonances in a final state with four leptons and missing transverse energy or jets. The search uses proton-proton collision data at a centre-of-mass energy of 13 TeV collected by the ATLAS detector from 2015 to 2018 at the Large Hadron Collider with a total integrated luminosity of 139 fb^{-1}. The search focused on two signal processes: $R \to SH \to 4\ell + E_{\mathrm{T}}^{\mathrm{miss}}$ and $A \to ZH \to 4\ell + X$. For the $R \to SH \to 4\ell + E_{\mathrm{T}}^{\mathrm{miss}}$ signal, the R boson decays to S and H bosons, where $S \to \nu\nu$ and $H \to ZZ \to 4\ell$. In the $A \to ZH \to 4\ell + X$ signal, the A boson decays to Z and H bosons, with two possible decay modes considered for the associated Z and H bosons: $A \to Z(\to \ell^+\ell^- / j\bar{j} / \nu\bar{\nu})H(\to 4\ell)$

and $A \to Z(\to 2\ell)H(\to 2\ell + j\bar{j}/\nu\bar{\nu})$. For both the $A \to ZH \to 4\ell + X$ and $R \to SH \to 4\ell + E_{\mathrm{T}}^{\mathrm{miss}}$ processes, the heavy boson H mass is between 220 GeV to 1000 GeV. The mass range considered for the hypothetical resonance is between 320–1300 GeV for the A boson and 390–1300 GeV for the R boson, while the S boson mass is fixed to 160 GeV.

No significant deviation above the SM backgrounds is observed. The highest excess observed in the data is at $(m_A, m_H) = (510, 380)$ GeV mass point with 2.5σ for the $A \to ZH \to 4\ell + X$. A few accesses at several (m_R, m_H) and (m_A, m_H) mass hypotheses are reported for the $R \to SH \to 4\ell + E_{\mathrm{T}}^{\mathrm{miss}}$ and $A \to ZH \to 4\ell + X$ signals with significance around 2σ. The results were translated into upper limits on the $\sigma(gg \to R) \times \mathcal{B}(R \to SH \times \mathcal{B}(H \to ZZ) \times \mathcal{B}(ZZ \to 4\ell)$ and $\sigma(gg \to A) \times \mathcal{B}(A \to ZH) \times \mathcal{B}(H \to ZZ) \times \mathcal{B}(ZZZ \to 4\ell)$ at 95% confidence. For the $R \to SH \to 4\ell + E_{\mathrm{T}}^{\mathrm{miss}}$ signal, the observed (expected) upper limits range from 0.031–0.539 (0.034–0.343) fb for $(m_R, m_H) = (390, 220)$ GeV to $(m_R, m_H) = (1300, 1000)$ GeV. For the $A \to ZH \to 4\ell + X$ signal, the observed (expected) upper limits range from 0.027–0.419 (0.035–0.335) fb for $(m_A, m_H) = (320, 220)$ GeV to $(m_A, m_H) = (1300, 1000)$ GeV.

Acknowledgements

We thank CERN for the very successful operation of the LHC, as well as the support staff from our institutions without whom ATLAS could not be operated efficiently.

We acknowledge the support of ANPCyT, Argentina; YerPhI, Armenia; ARC, Australia; BMWFW and FWF, Austria; ANAS, Azerbaijan; SSTC, Belarus; CNPq and FAPESP, Brazil; NSERC, NRC and CFI, Canada; CERN; CONICYT, Chile; CAS, MOST and NSFC, China; COLCIENCIAS, Colombia; MSMT CR, MPO CR and VSC CR, Czech Republic; DNRF and DNSRC, Denmark; IN2P3-CNRS, CEA-DRF/IRFU, France; SRNSFG, Georgia; BMBF, HGF, and MPG, Germany; GSRT, Greece; RGC, Hong Kong SAR, China; ISF and Benoziyo Center, Israel; INFN, Italy; MEXT and JSPS, Japan; CNRST, Morocco; NWO, Netherlands; RCN, Norway; MNiSW and NCN, Poland; FCT, Portugal; MNE/IFA, Romania; MES of Russia and NRC KI, Russian Federation; JINR; MESTD, Serbia; MSSR, Slovakia; ARRS and MIZŠ, Slovenia; DST/NRF, South Africa; MINECO, Spain; SRC and Wallenberg Foundation, Sweden; SERI, SNSF and Cantons of Bern and Geneva, Switzerland; MOST, Taiwan; TAEK, Turkey; STFC, United Kingdom; DOE and NSF, United States of America. In addition, individual groups and members have received support from BCKDF, CANARIE, CRC and Compute Canada, Canada; COST, ERC, ERDF, Horizon 2020, and Marie Sk lodowska-Curie Actions, European Union; Investissements d' Avenir Labex and Idex, ANR, France; DFG and AvH Foundation, Germany; Herakleitos, Thales and Aristeia programmes co-financed by EU-ESF and the Greek NSRF, Greece; BSF-NSF and GIF, Israel; CERCA Programme Generalitat de Catalunya, Spain; The Royal Society and Leverhulme Trust, United Kingdom.

The crucial computing support from all WLCG partners is acknowledged gratefully, in particular from CERN, the ATLAS Tier-1 facilities at TRIUMF (Canada), NDGF (Denmark, Norway, Sweden), CC-IN2P3 (France), KIT/GridKA (Germany), INFN-CNAF (Italy), NL-T1 (Netherlands), PIC (Spain), ASGC (Taiwan), RAL (UK) and BNL (USA), the Tier-2 facilities worldwide and large non-WLCG resource providers. Major contributors of computing resources are listed in Ref. [92].

A Signal region optimisation

The signal regions were defined depending on the number of jets, b-jets, the $p_{\mathrm{T}}^{4\ell}$ and the $E_{\mathrm{T}}^{\mathrm{miss}}$ significance. Figure 7 shows a flowchart for the signal regions' development.

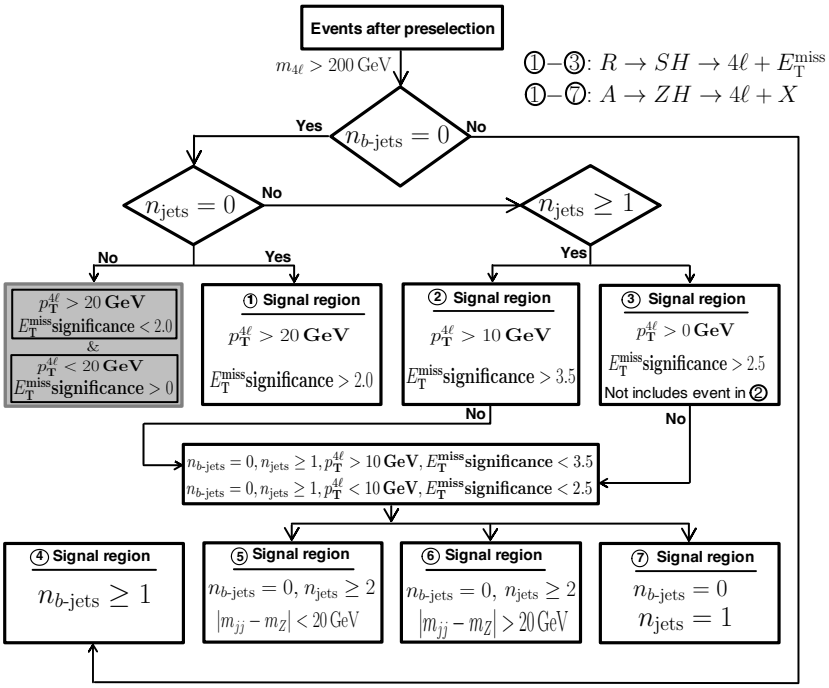

Figure 7: A flowchart diagram illustrates the signal regions for the $R \to SH \to 4\ell + E_{\mathrm{T}}^{\mathrm{miss}}$ and $A \to ZH \to 4\ell + X$ signals' optimisation. Three signal regions were developed for the $R \to SH \to 4\ell + E_{\mathrm{T}}^{\mathrm{miss}}$ signal, and seven signal regions for the $A \to ZH \to 4\ell + X$ signal.

B Local p_0 values

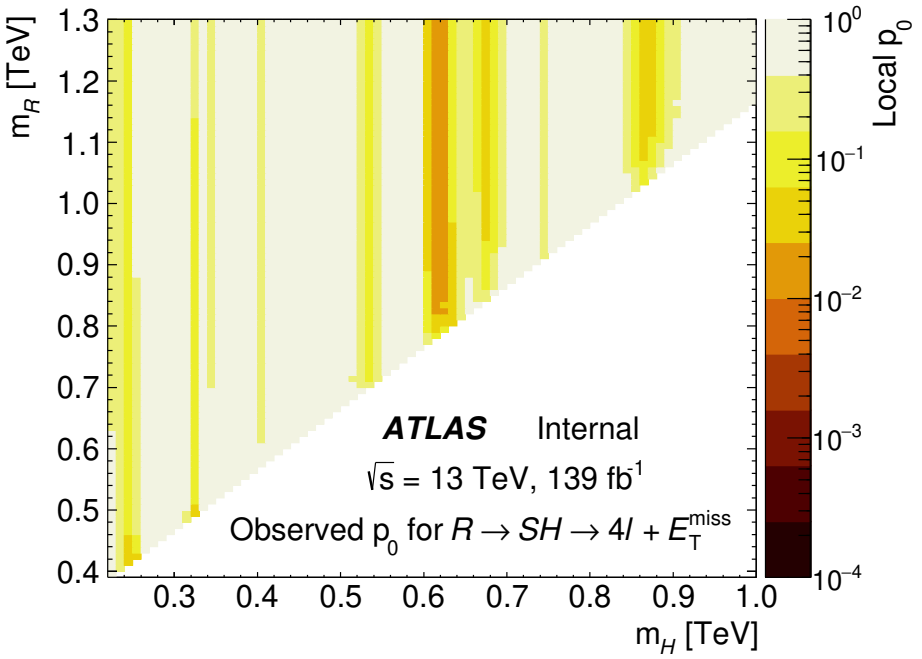

(a)

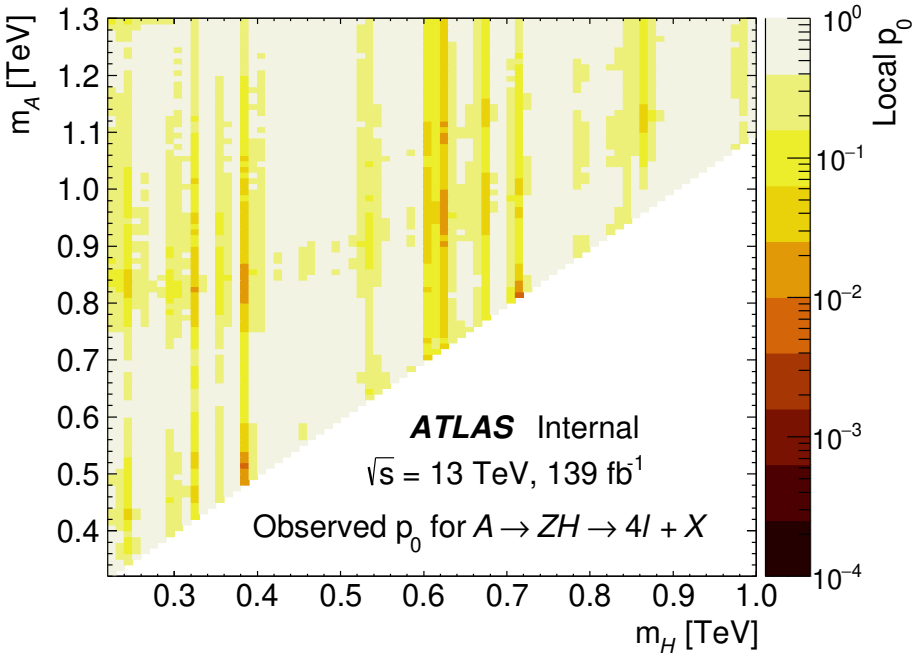

(b)

Figure 8: The local p_0 values on the two-dimensional contour of (m_H, m_A) plane for (b) the $A \to ZH \to 4\ell + X$ process, and on the (m_H, m_R) plane for (a) the $R \to SH \to 4\ell + E_{\mathrm{T}}^{\mathrm{miss}}$ process. The z-axis displays the local p_0 values

References

[1] ATLAS Collaboration, *Observation of a new particle in the search for the Standard Model Higgs boson with the ATLAS detector at the LHC*, Phys. Lett. B **716** (2012) 1, arXiv: 1207.7214 [hep-ex] (cit. on p. 2).

[2] CMS Collaboration, *Observation of a new boson at a mass of 125 GeV with the CMS experiment at the LHC*, Phys. Lett. B **716** (2012) 30, arXiv: 1207.7235 [hep-ex] (cit. on p. 2).

[3] ATLAS Collaboration, *Measurements of the Higgs boson production and decay rates and coupling strengths using pp collision data at $\sqrt{s}$ = 7 and 8 TeV in the ATLAS experiment*, Eur. Phys. J. C **76** (2016) 6, arXiv: 1507.04548 [hep-ex] (cit. on p. 2).

[4] ATLAS Collaboration, *Study of the spin and parity of the Higgs boson in diboson decays with the ATLAS detector*, Eur. Phys. J. C **75** (2015) 476, arXiv: 1506.05669 [hep-ex] (cit. on p. 2), Erratum: Eur. Phys. J. C **76** (2016) 152.

[5] CMS Collaboration, *Precise determination of the mass of the Higgs boson and tests of compatibility of its couplings with the standard model predictions using proton collisions at 7 and 8 TeV*, Eur. Phys. J. C **75** (2015) 212, arXiv: 1412.8662 [hep-ex] (cit. on p. 2).

[6] CMS Collaboration, *Constraints on the spin-parity and anomalous HVV couplings of the Higgs boson in proton collisions at 7 and 8 TeV*, Phys. Rev. D **92** (2015) 012004, arXiv: 1411.3441 [hep-ex] (cit. on p. 2).

[7] H. E. Haber and G. L. Kane, *The Search for Supersymmetry: Probing Physics Beyond the Standard Model*, Phys. Rept. **117** (1985) 75 (cit. on p. 2).

[8] N. Arkani-Hamed, S. Dimopoulos and G. R. Dvali, *The Hierarchy problem and new dimensions at a millimeter*, Phys. Lett. B **429** (1998) 263, arXiv: hep-ph/9803315 (cit. on p. 2).

[9] G. F. Giudice, *Naturally Speaking: The Naturalness Criterion and Physics at the LHC*, 2008, arXiv: 0801.2562 [hep-ph] (cit. on p. 2).

[10] G. C. Branco et al., *Theory and phenomenology of two-Higgs-doublet models*, Phys. Rept. **516** (2012) 1, arXiv: 1106.0034 [hep-ph] (cit. on p. 2).

[11] T. D. Lee, *A Theory of Spontaneous T Violation*, Phys. Rev. D **8** (1973) 1226, ed. by G. Feinberg (cit. on p. 2).

[12] S. von Buddenbrock et al., *Phenomenological signatures of additional scalar bosons at the LHC*, Eur. Phys. J. C **76** (2016) 580, arXiv: 1606.01674 [hep-ph] (cit. on pp. 2, 3).

[13] M. Muhlleitner, M. O. P. Sampaio, R. Santos and J. Wittbrodt, *The N2HDM under Theoretical and Experimental Scrutiny*, JHEP **03** (2017) 094, arXiv: 1612.01309 [hep-ph] (cit. on p. 2).

[14] S. von Buddenbrock et al., *Multi-lepton signatures of additional scalar bosons beyond the Standard Model at the LHC*, J. Phys. G **45** (2018) 115003, arXiv: 1711.07874 [hep-ph] (cit. on p. 3).

[15] A. G. Cohen, D. B. Kaplan and A. E. Nelson, *Progress in electroweak baryogenesis*, Ann. Rev. Nucl. Part. Sci. **43** (1993) 27, arXiv: hep-ph/9302210 (cit. on p. 3).

[16] ATLAS Collaboration, *Combination of searches for Higgs boson pairs in pp collisions at $\sqrt{s}$ =13 TeV with the ATLAS detector*, Phys. Lett. B **800** (2020) 135103, arXiv: 1906.02025 [hep-ex] (cit. on p. 3).

[17] CMS Collaboration, *Combination of searches for Higgs boson pair production in proton-proton collisions at $\sqrt{s}$ = 13 TeV*, Phys. Rev. Lett. **122** (2019) 121803, arXiv: 1811.09689 [hep-ex] (cit. on p. 3).

[18] ATLAS Collaboration, *Searches for heavy ZZ and ZW resonances in the $\ell\ell qq$ and $\nu\nu qq$ final states in pp collisions at $\sqrt{s}$ = 13 TeV with the ATLAS detector*, JHEP **03** (2018) 009, arXiv: 1708.09638 [hep-ex] (cit. on p. 3).

[19] ATLAS Collaboration, *Search for WW/WZ resonance production in $\ell\nu qq$ final states in pp collisions at $\sqrt{s}$ = 13 TeV with the ATLAS detector*, JHEP **03** (2018) 042, arXiv: 1710.07235 [hep-ex] (cit. on p. 3).

[20] ATLAS Collaboration, *Search for heavy diboson resonances in semileptonic final states in pp collisions at $\sqrt{s}$ = 13 TeV with the ATLAS detector*, Eur. Phys. J. C **80** (2020) 1165, arXiv: 2004.14636 [hep-ex] (cit. on p. 3).

[21] ATLAS Collaboration, *Search for diboson resonances in hadronic final states in 139 fb^{-1} of pp collisions at $\sqrt{s}$ = 13 TeV with the ATLAS detector*, JHEP **09** (2019) 091, [Erratum: JHEP 06, 042 (2020)], arXiv: 1906.08589 [hep-ex] (cit. on p. 3).

[22] CMS Collaboration, *Search for a heavy Higgs boson decaying to a pair of W bosons in proton-proton collisions at $\sqrt{s}$ = 13 TeV*, JHEP **03** (2020) 034, arXiv: 1912.01594 [hep-ex] (cit. on p. 3).

[23] CMS Collaboration, *Search for a new scalar resonance decaying to a pair of Z bosons in proton-proton collisions at $\sqrt{s}$ = 13 TeV*, JHEP **06** (2018) 127, [Erratum: JHEP 03, 128 (2019)], arXiv: 1804.01939 [hep-ex] (cit. on p. 3).

[24] ATLAS Collaboration, *Search for heavy resonances decaying into a W or Z boson and a Higgs boson in final states with leptons and b-jets in 36 fb^{-1} of $\sqrt{s}$ = 13 TeV pp collisions with the ATLAS detector*, JHEP **03** (2018) 174, [Erratum: JHEP 11, 051 (2018)], arXiv: 1712.06518 [hep-ex] (cit. on p. 3).

[25] CMS Collaboration, *Search for a heavy pseudoscalar Higgs boson decaying into a 125 GeV Higgs boson and a Z boson in final states with two tau and two light leptons at $\sqrt{s}$ = 13 TeV*, JHEP **03** (2020) 065, arXiv: 1910.11634 [hep-ex] (cit. on p. 3).

[26] CMS Collaboration, *Search for neutral resonances decaying into a Z boson and a pair of b jets or τ leptons*, Phys. Lett. B **759** (2016) 369, arXiv: 1603.02991 [hep-ex] (cit. on p. 3).

[27] A. M. Sirunyan et al., *Search for new neutral Higgs bosons through the $H \to ZA \to \ell^+\ell^-\mathrm{b\bar{b}}$ process in pp collisions at $\sqrt{s}$ = 13 TeV*, JHEP **03** (2020) 055, arXiv: 1911.03781 [hep-ex] (cit. on p. 3).

[28] ATLAS Collaboration, *Search for a heavy Higgs boson decaying into a Z boson and another heavy Higgs boson in the $\ell\ell bb$ final state in pp collisions at $\sqrt{s}$ = 13 TeV with the ATLAS detector*, Phys. Lett. B **783** (2018) 392, arXiv: 1804.01126 [hep-ex] (cit. on p. 3).

[29] ATLAS Collaboration, *Search for a heavy Higgs boson decaying into a Z boson and another heavy Higgs boson in the $\ell\ell bb$ and $\ell\ell WW$ final states in pp collisions at $\sqrt{s}$ = 13 TeV with the ATLAS detector*, Eur. Phys. J. C **81** (2021) 396, arXiv: 2011.05639 [hep-ex] (cit. on p. 3).

[30] ATLAS Collaboration, *The ATLAS Experiment at the CERN Large Hadron Collider*, JINST **3** (2008) S08003 (cit. on p. 4).

[31] ATLAS Collaboration, *Study of the mechanical stability of the ATLAS Insertable B-Layer*, ATL-INDET-PUB-2015-001, 2015, URL: https://cds.cern.ch/record/2022587 (cit. on p. 4).

[32] ATLAS Collaboration, *Performance of the ATLAS trigger system in 2015*, Eur. Phys. J. C **77** (2017) 317, arXiv: 1611.09661 [hep-ex] (cit. on p. 4).

[33] ATLAS Collaboration, *Operation and performance of the ATLAS semiconductor tracker*, JINST **9** (2014) P08009, arXiv: 1404.7473 [hep-ex] (cit. on p. 4).

[34] ATLAS Collaboration, *Monitoring and data quality assessment of the ATLAS liquid argon calorimeter*, JINST **9** (2014) P07024, arXiv: 1405.3768 [hep-ex] (cit. on p. 4).

[35] ATLAS Collaboration, *Selection of jets produced in* 13 *TeV proton–proton collisions with the ATLAS detector*, ATLAS-CONF-2015-029, 2015, URL: https://cds.cern.ch/record/2037702 (cit. on p. 4).

[36] ATLAS Collaboration, *The ATLAS Simulation Infrastructure*, Eur. Phys. J. C **70** (2010) 823, arXiv: 1005.4568 [physics.ins-det] (cit. on p. 4).

[37] S. Agostinelli et al., *GEANT4–a simulation toolkit*, Nucl. Instrum. Meth. A **506** (2003) 250 (cit. on p. 4).

[38] T. Sjostrand, S. Mrenna and P. Z. Skands, *A Brief Introduction to PYTHIA 8.1*, Comput. Phys. Commun. **178** (2008) 852, arXiv: 0710.3820 [hep-ph] (cit. on p. 4).

[39] ATLAS Collaboration, *Summary of ATLAS Pythia 8 tunes*, ATL-PHYS-PUB-2012-003, 2012, URL: https://cds.cern.ch/record/1474107 (cit. on p. 4).

[40] A. D. Martin, W. J. Stirling, R. S. Thorne and G. Watt, *Parton distributions for the LHC*, Eur. Phys. J. C **63** (2009) 189, arXiv: 0901.0002 [hep-ph] (cit. on p. 4).

[41] E. Bothmann et al., *Event Generation with Sherpa 2.2*, SciPost Phys. **7** (2019) 034, arXiv: 1905.09127 [hep-ph] (cit. on p. 4).

[42] R. D. Ball et al., *Parton distributions for the LHC Run II*, JHEP **04** (2015) 040, arXiv: 1410.8849 [hep-ph] (cit. on pp. 4, 5).

[43] S. Höche, F. Krauss, S. Schumann and F. Siegert, *QCD matrix elements and truncated showers*, JHEP **05** (2009) 053, arXiv: 0903.1219 [hep-ph] (cit. on pp. 4, 5).

[44] A. Denner, S. Dittmaier and L. Hofer, *Collier: a fortran-based Complex One-Loop LIbrary in Extended Regularizations*, Comput. Phys. Commun. **212** (2017) 220, arXiv: 1604.06792 [hep-ph] (cit. on p. 4).

[45] F. Buccioni et al., *OpenLoops 2*, Eur. Phys. J. C **79** (2019) 866, arXiv: 1907.13071 [hep-ph] (cit. on p. 4).

[46] F. Cascioli, P. Maierhöfer and S. Pozzorini, *Scattering Amplitudes with Open Loops*, Phys. Rev. Lett. **108** (2012) 111601, arXiv: 1111.5206 [hep-ph] (cit. on pp. 4, 5).

[47] S. Schumann and F. Krauss, *A Parton shower algorithm based on Catani-Seymour dipole factorisation*, JHEP **03** (2008) 038, arXiv: 0709.1027 [hep-ph] (cit. on p. 4).

[48] S. Höche, F. Krauss, M. Schönherr and F. Siegert, *QCD matrix elements + parton showers: The NLO case*, JHEP **04** (2013) 027, arXiv: 1207.5030 [hep-ph] (cit. on pp. 4, 5).

[49] B. Biedermann, A. Denner, S. Dittmaier, L. Hofer and B. Jäger, *Electroweak corrections to $pp \to \mu^+\mu^- e^+ e^- + X$ at the LHC: a Higgs background study*, Phys. Rev. Lett. **116** (2016) 161803, arXiv: 1601.07787 [hep-ph] (cit. on p. 4).

[50] B. Biedermann, A. Denner, S. Dittmaier, L. Hofer and B. Jager, *Next-to-leading-order electroweak corrections to the production of four charged leptons at the LHC*, JHEP **01** (2017) 033, arXiv: 1611.05338 [hep-ph] (cit. on p. 4).

[51] J. Alwall, M. Herquet, F. Maltoni, O. Mattelaer and T. Stelzer, *MadGraph 5 : Going Beyond*, JHEP **06** (2011) 128, arXiv: 1106.0522 [hep-ph] (cit. on p. 5).

[52] T. Sjöstrand et al., *An Introduction to PYTHIA 8.2*, Comput. Phys. Commun. **191** (2015) 159, arXiv: 1410.3012 [hep-ph] (cit. on p. 5).

[53] S. Alioli, P. Nason, C. Oleari and E. Re, *A general framework for implementing NLO calculations in shower Monte Carlo programs: the POWHEG BOX*, JHEP **06** (2010) 043, arXiv: 1002.2581 [hep-ph] (cit. on p. 5).

[54] R. D. Ball et al., *Impact of Heavy Quark Masses on Parton Distributions and LHC Phenomenology*, Nucl. Phys. B **849** (2011) 296, arXiv: 1101.1300 [hep-ph] (cit. on p. 5).

[55] ATLAS Collaboration, *ATLAS Pythia 8 tunes to 7 TeV data*, ATL-PHYS-PUB-2014-021, 2014, URL: https://cds.cern.ch/record/1966419 (cit. on p. 5).

[56] D. Berdine, N. Kauer and D. Rainwater, *Breakdown of the Narrow Width Approximation for New Physics*, Phys. Rev. Lett. **99** (2007) 111601, arXiv: hep-ph/0703058 (cit. on p. 5).

[57] T. Gleisberg, S. Höche, F. Krauss, M. Schönherr, S. Schumann et al., *Event generation with SHERPA 1.1*, JHEP **02** (2009) 007, arXiv: 0811.4622 [hep-ph] (cit. on p. 5).

[58] T. Gleisberg and S. Höche, *Comix, a new matrix element generator*, JHEP **12** (2008) 039, arXiv: 0808.3674 [hep-ph] (cit. on p. 5).

[59] F. Cascioli et al., *Precise Higgs-background predictions: merging NLO QCD and squared quark-loop corrections to four-lepton + 0,1 jet production*, JHEP **01** (2014) 046, arXiv: 1309.0500 [hep-ph] (cit. on p. 5).

[60] A. Denner, S. Dittmaier and L. Hofer, *COLLIER - A fortran-library for one-loop integrals*, PoS **LL2014** (2014) 071, arXiv: 1407.0087 [hep-ph] (cit. on p. 5).

[61] ATLAS Collaboration, *Electron and photon performance measurements with the ATLAS detector using the 2015–2017 LHC proton-proton collision data*, JINST **14** (2019) P12006, arXiv: 1908.00005 [hep-ex] (cit. on p. 6).

[62] ATLAS Collaboration, *Improved electron reconstruction in ATLAS using the Gaussian Sum Filter-based model for bremsstrahlung*, ATLAS-CONF-2012-047, 2012, URL: https://cds.cern.ch/record/1449796 (cit. on p. 6).

[63] ATLAS Collaboration, *Electron reconstruction and identification in the ATLAS experiment using the 2015 and 2016 LHC proton-proton collision data at $\sqrt{s} = 13$ TeV*, Eur. Phys. J. C **79** (2019) 639, arXiv: 1902.04655 [physics.ins-det] (cit. on pp. 6, 13).

[64] ATLAS Collaboration, *Muon reconstruction performance of the ATLAS detector in proton–proton collision data at $\sqrt{s}$ =13 TeV*, Eur. Phys. J. C **76** (2016) 292, arXiv: 1603.05598 [hep-ex] (cit. on pp. 6, 13).

[65] ATLAS Collaboration, *Jet reconstruction and performance using particle flow with the ATLAS Detector*, Eur. Phys. J. C **77** (2017) 466, arXiv: 1703.10485 [hep-ex] (cit. on p. 6).

[66] ATLAS Collaboration, *Topological cell clustering in the ATLAS calorimeters and its performance in LHC Run 1*, Eur. Phys. J. C **77** (2017) 490, arXiv: 1603.02934 [hep-ex] (cit. on p. 6).

[67] M. Cacciari, G. P. Salam and G. Soyez, *The anti-k_t jet clustering algorithm*, JHEP **04** (2008) 063, arXiv: 0802.1189 [hep-ph] (cit. on p. 6).

[68] ATLAS Collaboration, *Jet energy scale measurements and their systematic uncertainties in proton-proton collisions at $\sqrt{s}$ = 13 TeV with the ATLAS detector*, Phys. Rev. D **96** (2017) 072002, arXiv: 1703.09665 [hep-ex] (cit. on pp. 6, 13).

[69] ATLAS Collaboration, *Performance of pile-up mitigation techniques for jets in pp collisions at $\sqrt{s}$ = 8 TeV using the ATLAS detector*, Eur. Phys. J. C **76** (2016) 581, arXiv: 1510.03823 [hep-ex] (cit. on p. 6).

[70] ATLAS Collaboration, *Tagging and suppression of pileup jets with the ATLAS detector*, ATLAS-CONF-2014-018, 2014, URL: https://cds.cern.ch/record/1700870 (cit. on p. 6).

[71] ATLAS Collaboration, *ATLAS b-jet identification performance and efficiency measurement with $t\bar{t}$ events in pp collisions at $\sqrt{s}$ = 13 TeV*, Eur. Phys. J. C **79** (2019) 970, arXiv: 1907.05120 [hep-ex] (cit. on pp. 6, 7).

[72] ATLAS Collaboration, *Optimisation and performance studies of the ATLAS b-tagging algorithms for the 2017-18 LHC run*, ATL-PHYS-PUB-2017-013, 2017, URL: https://cds.cern.ch/record/2273281 (cit. on p. 6).

[73] The ATLAS Collaboration, *Recommendations of the Physics Objects and Analysis Harmonisation Study Groups 2014*, tech. rep. ATL-COM-PHYS-2014-451, CERN, 2014, URL: https://cds.cern.ch/record/1700874 (cit. on p. 7).

[74] M. Aaboud et al., *Performance of missing transverse momentum reconstruction with the ATLAS detector using proton-proton collisions at $\sqrt{s}$ = 13 TeV*, Eur. Phys. J. C **78** (2018) 903, arXiv: 1802.08168 [hep-ex] (cit. on p. 7).

[75] ATLAS Collaboration, *E_T^{miss} performance in the ATLAS detector using 2015–2016 LHC pp collisions*, ATLAS-CONF-2018-023, 2018, URL: https://cds.cern.ch/record/2625233 (cit. on p. 7).

[76] ATLAS Collaboration, *2015 start-up trigger menu and initial performance assessment of the ATLAS trigger using Run-2 data*, ATL-DAQ-PUB-2016-001, 2016, URL: https://cds.cern.ch/record/2136007 (cit. on p. 7).

[77] ATLAS Collaboration, *Trigger Menu in 2016*, ATL-DAQ-PUB-2017-001, 2017, URL: https://cds.cern.ch/record/2242069 (cit. on p. 7).

[78] V. Kostyukhin, *VKalVrt - package for vertex reconstruction in ATLAS.*, (2003) (cit. on p. 8).

[79] ATLAS Collaboration, *Search for an additional, heavy Higgs boson in the $H \to ZZ$ decay channel at $\sqrt{s}$ = 8 TeV in pp collision data with the ATLAS detector*, Eur. Phys. J. C **76** (2016) 45, arXiv: 1507.05930 [hep-ex] (cit. on p. 8).

[80] ATLAS Collaboration, *Search for heavy ZZ resonances in the $\ell^+\ell^-\ell^+\ell^-$ and $\ell^+\ell^-\nu\bar{\nu}$ final states using proton–proton collisions at $\sqrt{s}$ = 13 TeV with the ATLAS detector*, Eur. Phys. J. C **78** (2018) 293, arXiv: 1712.06386 [hep-ex] (cit. on p. 8).

[81] ATLAS Collaboration, *Search for heavy resonances decaying into a pair of Z bosons in the $\ell^+\ell^-\ell'^+\ell'^-$ and $\ell^+\ell^-\nu\bar{\nu}$ final states using 139 fb^{-1} of proton–proton collisions at $\sqrt{s}$ = 13 TeV with the ATLAS detector*, Eur. Phys. J. C **81** (2021) 332, arXiv: 2009.14791 [hep-ex] (cit. on p. 8).

[82] A. L. Read, *Linear interpolation of histograms*, Nucl. Instrum. Meth. A **425** (1999) 357 (cit. on p. 10).

[83] ATLAS Collaboration, *Luminosity determination in pp collisions at $\sqrt{s}$ = 13 TeV using the ATLAS detector at the LHC*, ATLAS-CONF-2019-021, 2019, URL: https://cds.cern.ch/record/2677054 (cit. on p. 12).

[84] W. Buttinger, *Using Event Weights to account for differences in Instantaneous Luminosity and Trigger Prescale in Monte Carlo and Data*, tech. rep. ATL-COM-SOFT-2015-119, CERN, 2015, URL: https://cds.cern.ch/record/2014726 (cit. on p. 12).

[85] E. T. et al., *E_T^{miss} performance in the ATLAS detector using 2015-2016 LHC p-p collisions*, tech. rep. ATL-COM-PHYS-2017-1732, CERN, 2017, URL: https://cds.cern.ch/record/2294891 (cit. on p. 13).

[86] A. Kalogeropoulos and J. Alwall, *The SysCalc code: A tool to derive theoretical systematic uncertainties*, 2018, arXiv: 1801.08401 [hep-ph] (cit. on p. 13).

[87] J. Butterworth et al., *PDF4LHC recommendations for LHC Run II*, J. Phys. G **43** (2016) 023001, arXiv: 1510.03865 [hep-ph] (cit. on p. 13).

[88] J. Bellm et al., *Herwig 7.0/Herwig++ 3.0 release note*, Eur. Phys. J. C **76** (2016) 196, arXiv: 1512.01178 [hep-ph] (cit. on p. 13).

[89] G. Cowan, K. Cranmer, E. Gross and O. Vitells, *Asymptotic formulae for likelihood-based tests of new physics*, Eur. Phys. J. C **71** (2011) 1554, arXiv: 1007.1727 [physics.data-an] (cit. on pp. 14, 15), Erratum: Eur. Phys. J. C **73** (2013) 2501.

[90] ATLAS Collaboration, *Formulae for Estimating Significance*, All figures including auxiliary figures are available at https://atlas.web.cern.ch/Atlas/GROUPS/PHYSICS/PUBNOTES/ATL-PHYS-PUB-2020-025, 2020, URL: https://cds.cern.ch/record/2736148 (cit. on pp. 16–18).

[91] A. L. Read, *Presentation of search results: the CL_S technique*, J. Phys. G **28** (2002) 2693 (cit. on p. 15).

[92] ATLAS Collaboration, *ATLAS Computing Acknowledgements*, ATL-GEN-PUB-2016-002, URL: https://cds.cern.ch/record/2202407 (cit. on p. 21).